J. Fluid Mech. (1994), vol. 271, pp. 55–85

Maintenance of continental boundary-layer shear through counter-gradient vorticity flux in a barotropic model

By JEAN-RAYMOND BIDLOT† AND MELVIN E. STERN
Department of Oceanography, Florida State University, Tallahassee, FL 32306-3048, USA

(Received 9 April 1993 and in revised form 3 January 1994)

The use of a classical eddy parametrization in the analysis of continental boundary currents leads to the diffusion of momentum and relative vorticity and fails to recognize that the relevant eddies are dominated by the conservation of potential vorticity, which in turn may produce an increase in the mean relative vorticity. To illustrate this effect, we examine a non-inflected barotropic shear flow destabilized by the cross-steam variation in the bottom topography of a continental slope. The finite-amplitude evolution of the waves is analysed in a simple model with a step-like bottom topography and with a piecewise-uniform potential vorticity distribution. The increase in maximum mean vorticity is computed for various values of the Rossby number and the topographic elevation, and it is suggested that a similar effect, taking into account the isopycnal topography as well as the isobaths, could maintain the large inshore shear of the Gulf Stream. Cross-shelf transport of different water 'types' (i.e. potential vorticity and passive tracers) are also computed and suggested to be pertinent to the more realistic oceanic problem involving baroclinic effects. The numerical calculation employs the well-known method of contour dynamics, and the Green's function appropriate for the step-like topography is derived.

1. Introduction

Continental boundary currents often exhibit a region of relatively strong cyclonic shear on their inshore side, as is the case for the Gulf Stream (Brooks & Niiler 1977; Brooks & Mooers 1977) where mean shear of the order of the Coriolis parameter can be observed over the continental slope. The shelf break region is also the site of strong eddy activities leading to the exchange of water with different physical, chemical, and biological properties between the deep and the shelf regions. See Ford, Longard & Banks (1952), Lee & Mayer (1977), Lee & Atkinson (1983), Lee, Yoder & Atkinson (1991) for the Gulf Stream and Sugimoto, Kimura & Miyaji (1988), and Qiu, Toda & Imosato (1990) for the Kuroshio. Stern (1991*a*, 1993) proposed that the inshore shear of a boundary current could be maintained by counter-gradient vorticity fluxes at the steep continental slope, rather than by a classical eddy diffusive parametrization, and the particular mechanism investigated involved a net cross-slope mass flux produced by downstream topographic variations.

A different kind of topographic mechanism is discussed here, namely that due to the instability of a laminar shear flow along a continental slope. Collings & Grimshaw (1980, 1984) have shown that cross-stream topography can destabilize non-inflected

---

† Present address: Management Unit of the Mathematical Models of the North Sea and Scheldt Estuary, 100 Gulledelle, B-1200 Brussels, Belgium.

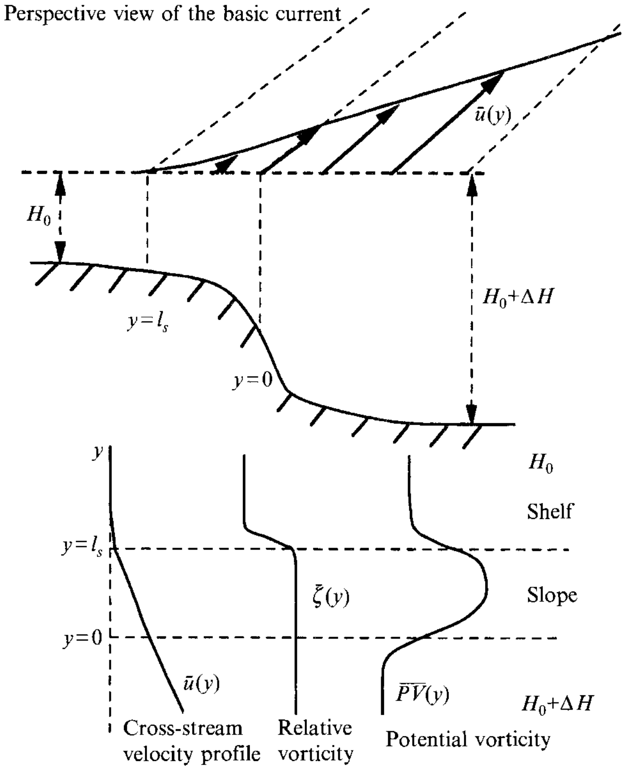

FIGURE 1. A laminar shear flow $\bar{u}(y)$ with monotonic vorticity $\bar{\zeta}(y)$ at the edge of a continental slope, of depth $h(y)$ which changes rapidly at the shelf break, such that the potential vorticity of this current $\overline{PV}(y) = (f+\bar{\zeta}(y))/h(y)$ has an extremum, where f is the constant Coriolis parameter.

barotropic currents which are otherwise stable. An illustration is provided by the flow in figure 1 which extends across the continental slope and onto a limited part of the shelf, with the corresponding relative vorticity decreasing monotonically to zero. Suppose that the cross-stream decrease in bottom depth is strong enough at the shelf break to produce the necessary potential vorticity maximum for a barotropic instability. If the condition is also sufficient, there will be a net eddy transport of water with maximum potential vorticity into the deep water thereby increasing the maximum mean vorticity in the shear flow by stretching of fluid columns displaced across the steep topography. Therefore any small tendency for lateral eddy diffusion of relative vorticity could be compensated by these topographically dominated effects at the continental slope.

For simplicity, we will consider a piecewise-constant shear flow $\bar{u}(y)$ and a step-like topography, for which case a detailed linear instability calculation is available (Appendix A). In this model (figure 6), a high-potential-vorticity layer of width l_s on the shelf separates lower-potential-vorticity fluids on the semi-infinite shelf from the semi-infinite deep region (having the same *relative* vorticity) on the other side of the escarpment ($y = 0$). We shall see that the evolution of the disturbance is quantitatively similar to the roll up of cores as in the classical *inflected* shear flow problem (Pozrikidis & Higdon 1985; Pratt & Pedlosky 1991), but now a qualitatively different effect on the mean vorticity occurs, namely vorticity can be transported up the mean gradient.

Pozrikidis & Higdon (1987) showed that the instability of two adjoining vortex layers leads to the rapid formation of widely spread vorticity cores. Bidlot (1993) considered the same problem for a wall jet, and figure 2 illustrates that even without dissipative processes a rapid diffusion of mean momentum and vorticity occurs. However, as will be seen, the presence of cross-stream topography in continental boundary currents has a profound effect on the eddies and the velocity profile. In fact, the restoring topographic force prevents the current from diffusing to the beach, and the conservation of potential vorticity increases or maintains the maximum mean vorticity.

The nonlinear stability calculation uses the well-known contour dynamical method (Zabusky, Hughes & Roberts, 1979), with a novel feature presented by the topography which requires the computation of the appropriate Green's function (§2). From this the stream function as well as the velocity components can be computed for any disturbance, leading to integral-differential equations which govern the evolution of the potential vorticity fronts.

The topography discontinuities in our model raise novel technical considerations relative to the implementation of contour dynamics, which are analysed in §3. Most of the initial conditions for the main calculations (§4) are the normal modes of the linear problem, starting with the mode of maximum growth rate, but some calculations with different scales are also given in §5. In all runs, the growth of an initially small-amplitude wave causes the flow to break up into a series of constant-potential-vorticity pools (cores) surrounded by irrotational as well as deep water. Computation was carried out long enough such that the new approximately steady mean vorticity field could be computed. 'Entrainment' is defined and computed as the volumetric transfer across the 'new' interfaces of the shear flow.

Wang (1992) also used a step-like topography in a barotropic contour dynamical model to study the interaction of a deep water eddy with a continental slope in the *absence* of a basic current, and was able to illustrate some important shelf processes such as cross-topographic exchange, topography eddy formation, vortex propagation and topographic trapped waves, but his study did not cover the effect of the cross-stream topography on the mean flow as discussed above. In addition, topographic instability was also considered in the contour dynamical calculation of Send (1989) but the investigated mechanism was due to *relative* vorticity extrema in the basic state and the flux was down-gradient. Grimshaw & Yi (1991) also used contour dynamics to discuss cross-stream topographic effects but did not address the instability problem. Finally, some relevant contour dynamical examples of shedding of eddies by localized topographic features like sea mounts have been analysed by several authors (Kozlov 1983; Thompson 1993).

2. Topographic Green's function

The Green's function derived by Wang (1992) is similar to ours and was developed at the same time, but an explicit derivation was not presented and this will be supplied here, along with a physical discussion involving the method of images.

2.1. *Green's function for a vortex near an escarpment*

We need to find the stream function induced by the vorticity ζ in an element of area $(\mathrm{d}\xi\,\mathrm{d}\eta)$ surrounding a point (ξ, η), with circulation $\Gamma = \zeta\,\mathrm{d}\xi\,\mathrm{d}\eta$. The instantaneous flow produced by such a point vortex (figure 3) on either side of the escarpment ($y = 0$), is irrotational and non-divergent. The connection conditions at $y = 0$ were formally derived by Spitz & Nof (1991) and simply require continuity of the mass flux

$$[vH] \equiv v(0^+)\,H_0 - v(0^-)(H_0 + \Delta H) = 0, \qquad (2.1)$$

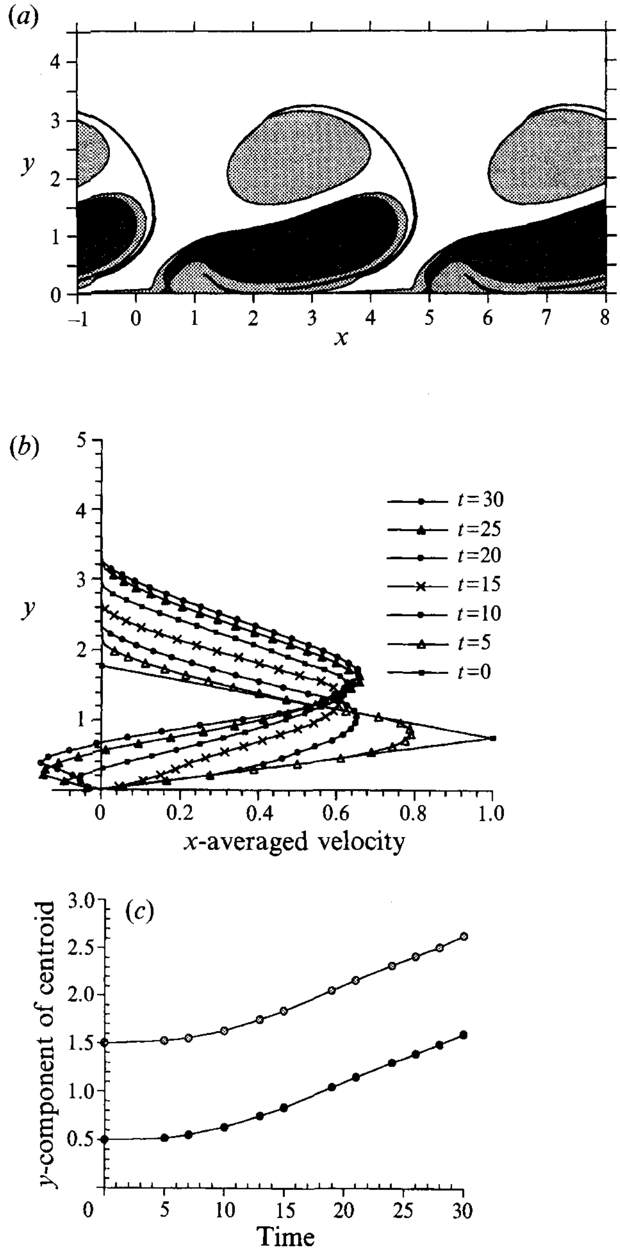

FIGURE 2. Reproduced from Bidlot (1993): An inviscid piecewise-linear barotropic wall jet ($t = 0$) in a flat-bottom ocean was perturbed by the most unstable linear mode. The maximum undisturbed jet velocity is unity, the vorticity in the cyclonic layer is also unity and $\zeta_2 < 0$ is the vorticity in the layer near the wall. (*a*) $\zeta_2 = -\frac{4}{3}$. The unstable evolution of the jet leads at $t = 25$ to the formation of vortex pairs which contain most of the fluid initially in the vortex layers (where the light and dark shaded areas respectively correspond to the cyclonic and anticyclonic fluid). (*b*) $\zeta_2 = -\frac{4}{3}$. The downstream velocity profile averaged over one wavelength shows a net diffusion of momentum and vorticity as the jet widens with time as well as a significant flow reversal region along the boundary with a lateral extent comparable to the initial ($t = 0$) width of the anticyclonic layer. (*c*) A wider jet with $\zeta_2 = -1$ yielded similar results to those above. The top curve is the ordinate of the centroid of the fluid with cyclonic vorticity, similarly the lower one corresponds to the anticyclonic part of the dipole. The curves show the tendency for the dipolar eddies which arise from the instability to propagate to large distances from the wall.

and finite vorticity across the step or continuity of u

$$[u] \equiv u(0^+) - u(0^-) = 0, \tag{2.2}$$

where u and v are respectively the along- and cross-escarpment velocity components and $[F]$ indicates that the limit of the difference between the value of F on each side of $y = 0$ is taken. In each region, let $u = u_0 + u_1$, $v = v_0 + v_1$, $\psi = \psi_0 + \psi_1$, where $(u_0, v_0) = (-\partial\psi_0/\partial y, \partial\psi_0/\partial x)$ is defined as the velocity field that would be produced if the depth were uniform, and $(u_1, v_1) = (-\partial\psi_1/\partial y, \partial\psi_1/\partial x)$ the residual. ψ_0 is the classical two-dimensional stream function induced by a point vortex of strength Γ, located at (ξ, η) as given by

$$\psi_0(x,y) = \frac{\Gamma}{4\pi} \ln\left[(x-\xi)^2 + (y-\eta)^2\right]. \tag{2.3}$$

Since the flow is irrotational and non-divergent at all $y \neq 0$, the residual velocity component v_1 must satisfy

$$\nabla^2 v_1 = 0. \tag{2.4}$$

Similarly the connection conditions (2.1) and (2.2) become

$$v_0(x,0)[H] + [v_1 H] = 0 \tag{2.5}$$

and

$$[u_1] = \left[\frac{\partial u_1}{\partial x}\right] = \left[-\frac{\partial v_1}{\partial y}\right] = 0. \tag{2.6}$$

The solution of (2.4) that satisfies (2.6) is

$$v_1 = \frac{1}{2\pi} \operatorname{Im}\left\{\int_0^\infty \mathrm{d}k\, \mathrm{e}^{\mathrm{i}kx} B(k)\, \mathrm{e}^{-k|y|} \operatorname{sgn}(y)\right\} \tag{2.7}$$

where

$$\operatorname{sgn}(y) = \begin{cases} +1, & y > 0 \\ -1, & y < 0. \end{cases}$$

$B(k)$ must be chosen to satisfy (2.5), or

$$\frac{\partial\psi_0(x,0)}{\partial x}[H] + [v_1 H] = 0. \tag{2.8}$$

By substituting (2.3), (2.7) in (2.8), and using the identity

$$\operatorname{Im}\left\{\int_0^\infty \mathrm{d}k\, \mathrm{e}^{\mathrm{i}k(x-\xi)}\, \mathrm{e}^{-k|\eta|}\right\} = \frac{x-\xi}{(x-\xi)^2 + \eta^2} \tag{2.9}$$

we get

$$B(k) = \frac{\Gamma \Delta H}{2H_0 + \Delta H} \mathrm{e}^{-\mathrm{i}k\xi} \mathrm{e}^{-k|\eta|}. \tag{2.10}$$

Then (2.7) gives

$$v_1(x,y) = \frac{\Gamma}{2\pi} \frac{\Delta H}{2H_0 + \Delta H} \frac{(x-\xi)\operatorname{sgn}(y)}{(x-\xi)^2 + (|y| + |\eta|)^2} \tag{2.11}$$

and the associated stream function is

$$\psi_1(x,y) = \frac{\Gamma}{4\pi} \frac{E}{2+E} \operatorname{sgn}(y) \ln\left[(x-\xi)^2 + (|y| + |\eta|)^2\right], \tag{2.12}$$

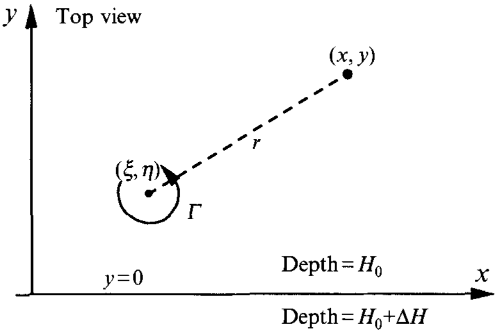

FIGURE 3. A point vortex of strength Γ is located at $(\xi, \eta \neq 0)$ on one side of an escarpment $(y = 0)$ modelled by two regions of constant depth. We are interested in the instantaneous velocity induced at any point (x, y).

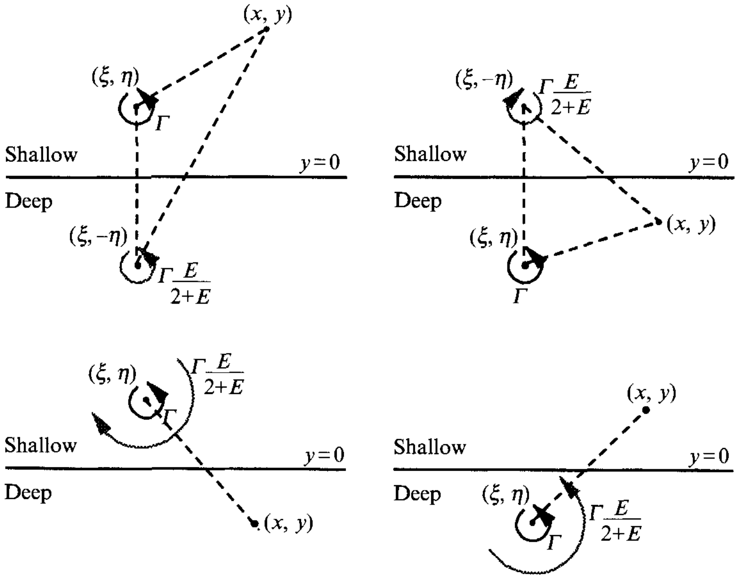

FIGURE 4. The flow field for the escarpment problem is equivalent to a constant-depth problem in which an image vortex (light arrow) is introduced to account for the step-like topography. The original point vortex of strength Γ is located at $(\xi, \eta \neq 0)$ and would produce a flow field at (x, y) given by (2.3) if the depth were uniform. The correction due to the presence of the escarpment is given by (2.12) and can be viewed as a point vortex of strength $\Gamma[E/(2+E)]\,\mathrm{sgn}(y)$ located at $(\xi, -\eta\,\mathrm{sgn}(\eta)\,\mathrm{sgn}(y))$. Four locations of the latter are possible depending on the relative position of both the forcing and the point of interest as shown above.

where $E = \Delta H/H_0$. Note that the field ψ_1 (2.12) which is to be added to (2.3) is equivalent to the field produced in a uniform-depth fluid by an image vortex of strength $\Gamma_1 = \Gamma E/(2+E)\,\mathrm{sgn}\,(y)$, located at a point $(\xi, -\eta\,\mathrm{sgn}\,(\eta)\,\mathrm{sgn}\,(y))$.

Depending on the respective locations of the initial point vortex (ξ, η) and the point of interest (x, y) four scenarios for the position of the image vortex are possible as sketched in figure 4. The image vortex has an ordinate equal and opposite to the initial vortex if y and η lie on the same side of the escarpment, otherwise the vortices coincide and the image strength $\Gamma E/(2+E)$ reinforces (interferes) with the initial vortex if the latter lies in a deep (shallow) region.

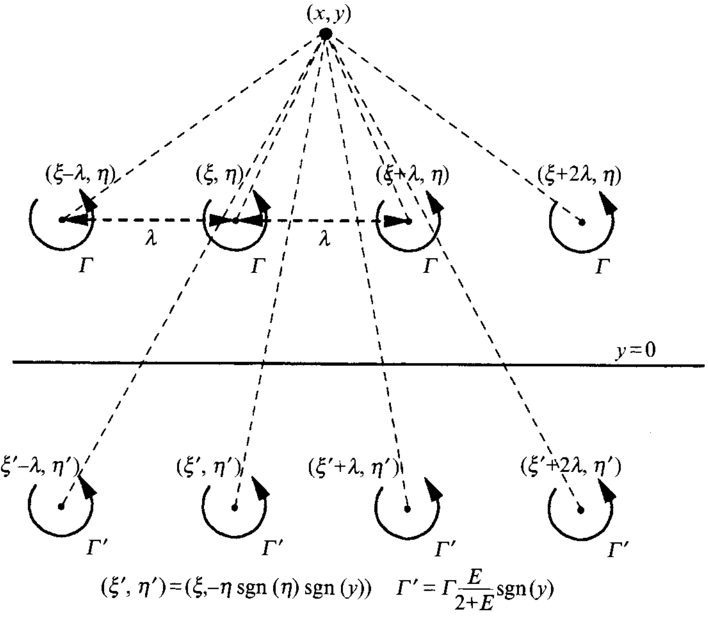

FIGURE 5. The flow field problem for a row of point vortices of strength Γ, parallel to the escarpment is equivalent to a flat-bottom problem if a row of image vortices of strength $\Gamma' = \Gamma[E/(2+E)]\,\mathrm{sgn}(y)$ is introduced. The image row will be located at the same place as the original row or at its mirror image depending on the position of the point of interest (x, y) as shown above.

2.2. *Green's function for downstream periodicity*

If the initial vortex is replaced by a row of periodic point vortices parallel to the escarpment (figure 5), then the sum of the influence of these (Lamb 1932) gives the result

$$\psi_0(x,y) = \frac{\Gamma}{4\pi}\ln\left[\sin^2\left(\frac{\pi}{\lambda}(x-\xi)\right)+\sinh^2\left(\frac{\pi}{\lambda}(y-\eta)\right)\right], \tag{2.13}$$

$$\psi_1(x,y) = \frac{\Gamma}{4\pi}\frac{E}{2+E}\,\mathrm{sgn}\,(y)\ln\left[\sin^2\left(\frac{\pi}{\lambda}(x-\xi)\right)+\sinh^2\left(\frac{\pi}{\lambda}(|y|+|\eta|)\right)\right], \tag{2.14}$$

corresponding to (2.3) and (2.12), where λ is the distance between two successive point vortices, and $\psi = \psi_0+\psi_1$ is the total Green's function for a periodic problem.

3. Formulation of the nonlinear stability problem

The very simple basic flow $\bar{u}$ in figure 6 has constant vorticity $\bar{\zeta}$ beyond the edge $(y < l_s)$ which is located on the shelf in shallow water. The mid layer $(0 \leqslant y \leqslant l_s)$ has a larger potential vorticity than either the $y > l_s$ of the $y < 0$ layer thereby satisfying the necessary condition for instability. For periodic disturbances of wavelength λ, there are three regions of uniform potential vorticity, separated by two interfaces $L_1(x, t)$ and $L_2(x, t)$. Conservation of potential vorticity requires that any fluid column advected across $y = 0$ or $y = l_s$ will generate vorticity anomalies ζ' relative to $\bar{\zeta}$. For example (figure 7*a*), any fluid particle which is advected from the irrotational region to a region $0 < y < l_s$ where the background vorticity is equal to $\bar{\zeta}$ has an anomaly $\zeta' = -\bar{\zeta}$. Moreover if the parcel crosses the escarpment (i.e. $y < 0$), stretching of the water column produces an increase in relative vorticity equal to Ef, in which case the anomaly

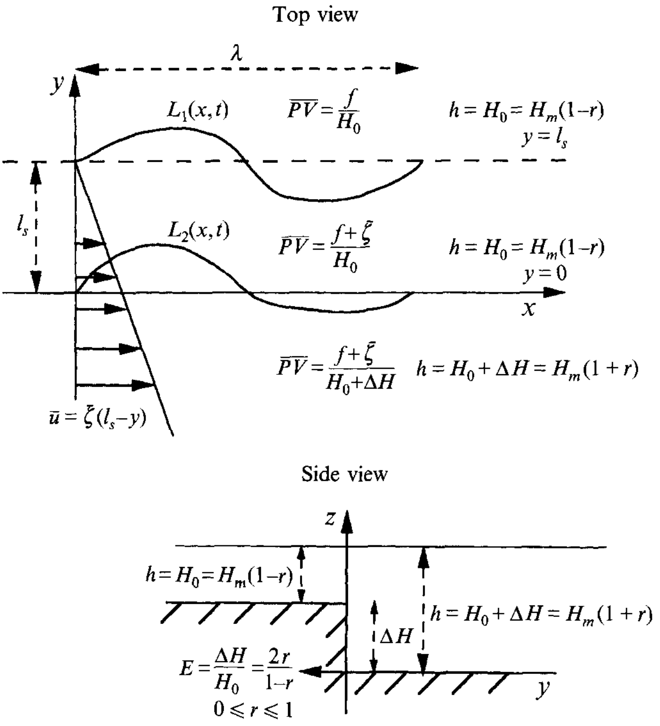

FIGURE 6. Escarpment limit of figure 1, in which a piecewise-uniform shear flow $\bar{u}(y)$ has its edge on the shelf (depth $= H_0$) at a distance $y = l_s$ from the escarpment ($y = 0$). Periodic disturbances with wavelength λ produce three layers of uniform potential vorticity ($\overline{PV}$) separated by two interfaces $L_1(x,t), L_2(x,t)$.

is $\zeta' = Ef - \bar{\zeta}$. A similar procedure can be followed for fluid particles displaced from the deep region as they first encounter the step and then the irrotational region. The different values of ζ' are summarized in figure 7(*a*). These anomalies will induce velocities which when added to the undisturbed shear flow $\bar{u}$ give the rate of displacement of the L_1, L_2 fronts.

It is convenient to split the problem of computing those instantaneous velocities into two simpler ones (figure 7*b*), each of which contains only one interface. Since the combined spatial distribution of ζ' from both problems is equivalent to the original problem, the sum of the velocity components from both problems is equivalent to the corresponding velocities in the original problem. The endpoints of each contour (figure 7) are connected by an horizontal segment to form a closed contour containing all non-zero anomalies for the problem in question.

In problem 2, the vorticity anomalies are

$$\zeta_3' = \frac{-E(\bar{\zeta}+f)}{1+E} \quad \text{for} \quad y > 0, \tag{3.1}$$

$$\zeta_4' = E(\bar{\zeta}+f) \quad \text{for} \quad y < 0, \tag{3.2}$$

and the velocity anomalies induced at any (x, y) are obtained by summing the effect of all vorticity anomalies. Consider (figure 8) any infinitesimal element of area $\mathrm{d}\xi\,\mathrm{d}\eta$ surrounding a point (ξ, η) within the area (C_2^+) bounded by $L_2 > 0$ and $y = 0$ (shaded area), and all the periodically displaced counterparts at $(\xi + k\lambda, \eta)$, $k = \pm 1, \pm 2 \ldots$. These elements have a constant vorticity anomaly ζ_3', therefore they induce a

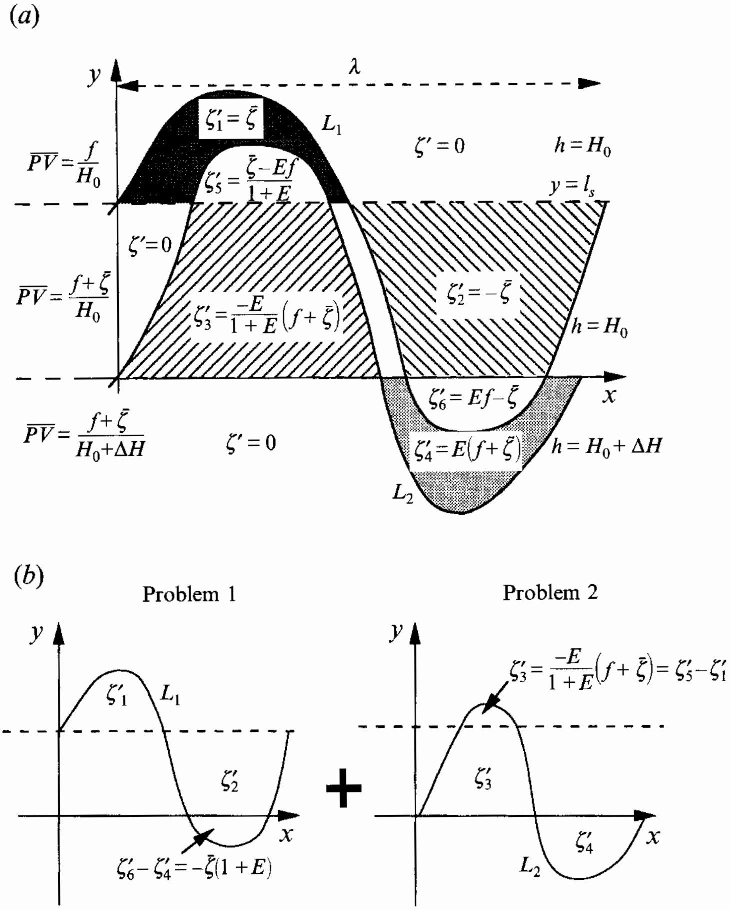

FIGURE 7. (*a*) Schematic representation of the vorticity anomalies generated when water columns are advected across $y = 0$ and $y = l_s$ by any disturbance L_1 and L_2. (*b*) The computation of the instantaneous velocities is split into two simpler problems with only one interface each. Problem 1 considers the field associated with the three vorticity anomalies ζ'_1, ζ'_2, $(\zeta'_6 - \zeta'_4)$ enclosed by L_1 and the horizontal segment $y = l_s$. Similarly problem 2 examines the field produced by the two vorticity anomalies ζ'_3 and ζ'_4 enclosed by L_2 and $y = 0$. When the figure for problem 2 is overlapped with that for problem 1, the sum of the vorticities yields the total anomalies in (*a*).

circulation $\Gamma = \zeta'_3 \,\mathrm{d}\xi\, \mathrm{d}\eta$ corresponding to a row of periodic point vortices of strength Γ on the line $y = \eta$, for which the corresponding stream function is the sum of (2.13) and (2.14). We integrate over the area bounded by C_2^+ to get the effect of all vorticity anomalies ζ'_3 and do likewise for the contribution of the vorticity anomalies ζ'_4 bounded by C_2^- (figure 8), thereby obtaining

$$\psi_2(x,y) = \psi_{20}(x,y) + \psi_{21}(x,y),$$

$$\psi_{20}(x,y) = \frac{1}{4\pi}\zeta'_3 \iint_{C_2^+} \mathrm{d}\xi\, \mathrm{d}\eta\, G(x-\xi, y-\eta) + \frac{1}{4\pi}\zeta'_4 \iint_{C_2^-} \mathrm{d}\xi\, \mathrm{d}\eta\, G(x-\xi, y-\eta), \tag{3.3}$$

$$\psi_{21}(x,y) = \frac{1}{4\pi}\zeta'_3 \frac{E}{2+E}\operatorname{sgn}(y) \iint_{C_2^+} \mathrm{d}\xi\, \mathrm{d}\eta\, G(x-\xi, y+\eta \operatorname{sgn}(\eta)\operatorname{sgn}(y))$$

$$+ \frac{1}{4\pi}\zeta'_4 \frac{E}{2+E}\operatorname{sgn}(y) \iint_{C_2^-} \mathrm{d}\xi\, \mathrm{d}\eta\, G(x-\xi, y+\eta \operatorname{sgn}(\eta)\operatorname{sgn}(y)), \tag{3.4}$$

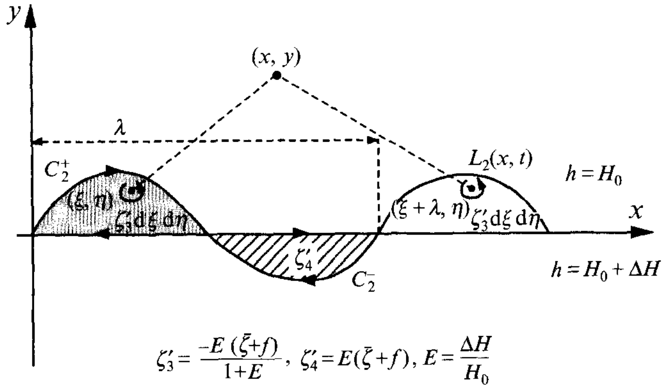

FIGURE 8. The flow field at (x, y) produced by a periodic disturbance can be obtained in problem 2 by summing the contribution of each vorticity element centred at (ξ, η) with circulation $\zeta_3' \mathrm{d}\xi \mathrm{d}\eta$ contained in C_2^+ as well as their periodic counterparts, and likewise for $\zeta_4' \mathrm{d}\xi \mathrm{d}\eta$ in C_2^-.

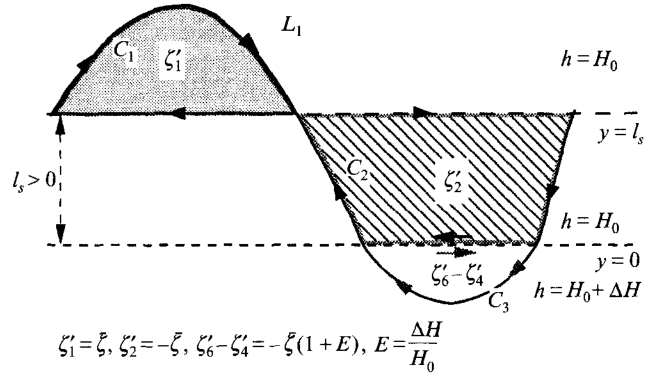

FIGURE 9. In problem 1, the vorticity anomalies have three possible values: ζ_1' if $L_1 > l_s$, ζ_2' if $0 < L_1 < l_s$ and $(\zeta_6' - \zeta_4')$ if $L_1 < 0$, respectively bounded by the closed contours C_1, C_2, and C_3.

where
$$G(x-\xi, y-\eta) = \ln\left[\sin^2\left(\frac{\pi}{\lambda}(x-\xi)\right) + \sinh^2\left(\frac{\pi}{\lambda}(y-\eta)\right)\right]$$
is the periodic Green's function. The velocity components are obtained by differentiating (3.3) and (3.4), i.e.
$$[u_{2i}(x,y), \quad v_{2i}(x,y)] = \left[-\frac{\partial \psi_{2i}}{\partial y}, \frac{\partial \psi_{2i}}{\partial x}\right], \quad i = 0, 1.$$
Then Green's theorem can be used to obtain contour integrals which are solved numerically, the actual expressions for which can be found in Appendix B.

Problem 1 is a little more difficult because if $L_1 < 0$ the vorticity anomalies at $y < l_s$ can have two different values as shown in figure 7(*b*). In that case, the three vorticity anomalies ζ_1', ζ_2' and $\zeta_6' - \zeta_4'$ are respectively bounded by the closed contours C_1, C_2, C_3 as represented in figure 9 for a periodic disturbance. The contribution ψ_{1i} of the L_1-anomalies is composed of two parts: ψ_{10} (the 'constant-depth' part) and ψ_{11} (the 'image' part). This can be expressed as
$$\psi_{1i} = \frac{1}{4\pi} ce_i \left\{ \sum_{k=1}^{2} \left[\zeta_k' \iint_{C_k} \mathrm{d}\xi \, \mathrm{d}\eta \, G(x-\xi, y-\eta_i) \right] + (\zeta_6' - \zeta_4') \iint_{C_3} \mathrm{d}\xi \, \mathrm{d}\eta \, G(x-\xi, y-\eta_i) \right\}, \tag{3.5}$$

where

$$ce_i = \begin{cases} 1, & i=0 \\ \dfrac{E}{2+E}\operatorname{sgn}(y), & i=1, \end{cases} \tag{3.6}$$

$$\eta_i = \eta_i(\eta) = \begin{cases} \eta, & i=0 \\ -\eta\operatorname{sgn}(\eta)\operatorname{sgn}(y), & i=1. \end{cases} \tag{3.7}$$

Note that if $L_1 > 0$ everywhere the C_3 domain in figure 9 disappears and the last term in (3.5) is zero. The velocity components $[u_{1i}(x,y), v_{1i}(x,y)]$, $i = 0, 1$ are obtained by differentiating (3.5) and the resulting area integrals are transformed to line integrals using Green's theorem. The integrals around C_1, C_2, C_3 are rearranged to give integrals along the entire L_1, the segment $y = l_s$ and that portion of $y = 0$ which intersects L_1. These intricate expressions are presented in Appendix B.

Finally, the velocity components at any point $(x, y \neq 0)$ are given by the combination of the two problems plus the action of the basic state $\bar{u}$, i.e.

$$\left.\begin{aligned} u(x,y) &= \bar{u}+u_{10}+u_{11}+u_{20}+u_{21}, \\ v(x,y) &= v_{10}+v_{11}+v_{20}+v_{21}, \end{aligned}\right\} \tag{3.8}$$

$$\bar{u}(y) = \begin{cases} 0, & y > l_s \\ \zeta(l_s - y), & y < l_s. \end{cases} \tag{3.9}$$

These velocities are evaluated on the L_1 and L_2 contours to compute the position of the interfaces at later time using the following set of Lagrangian integral-differential equations for the motion of any interfacial point $[x_j(t), L_m(x_j, t)], m = 1, 2$:

$$\left.\begin{aligned} \frac{\mathrm{d}x_j(t)}{\mathrm{d}t} &= u(x_j, L_m(x_j, t)), \\ \frac{\mathrm{d}L_m(x_j, t)}{\mathrm{d}t} &= v(x_j, L_m(x_j, t)). \end{aligned}\right\} \tag{3.10}$$

Except when mentioned otherwise, the equations were non-dimensionalized using the Coriolis parameter (f) as the reciprocal of the timescale. A special difficulty which arises in solving this system occurs when a $[x_j, L_m(x_j)]$ point crosses $y = 0$ where v is discontinuous. The resolution of this problem and other numerical considerations are discussed in Appendix C. The results are discussed next.

4. Numerical results

The initial perturbation was the most unstable normal mode of the linear theory (except as stated otherwise), with the interfaces at $t = 0$ given by

$$\left.\begin{aligned} L_1 &= l_s + A\cos\left(\frac{2\pi}{\lambda}x\right), \\ L_2 &= \begin{cases} A\,|L_{12}|\cos\left(\dfrac{2\pi}{\lambda}x+\theta_{12}\right), & L_2 > 0 \\ \dfrac{A\,|L_{12}|}{1+E}\cos\left(\dfrac{2\pi}{\lambda}x+\theta_{12}\right), & L_2 < 0, \end{cases} \\ A &\ll l_s, \end{aligned}\right\} \tag{4.1}$$

where $|L_{12}|$ and θ_{12} are respectively the relative amplitude and the phase shift (as

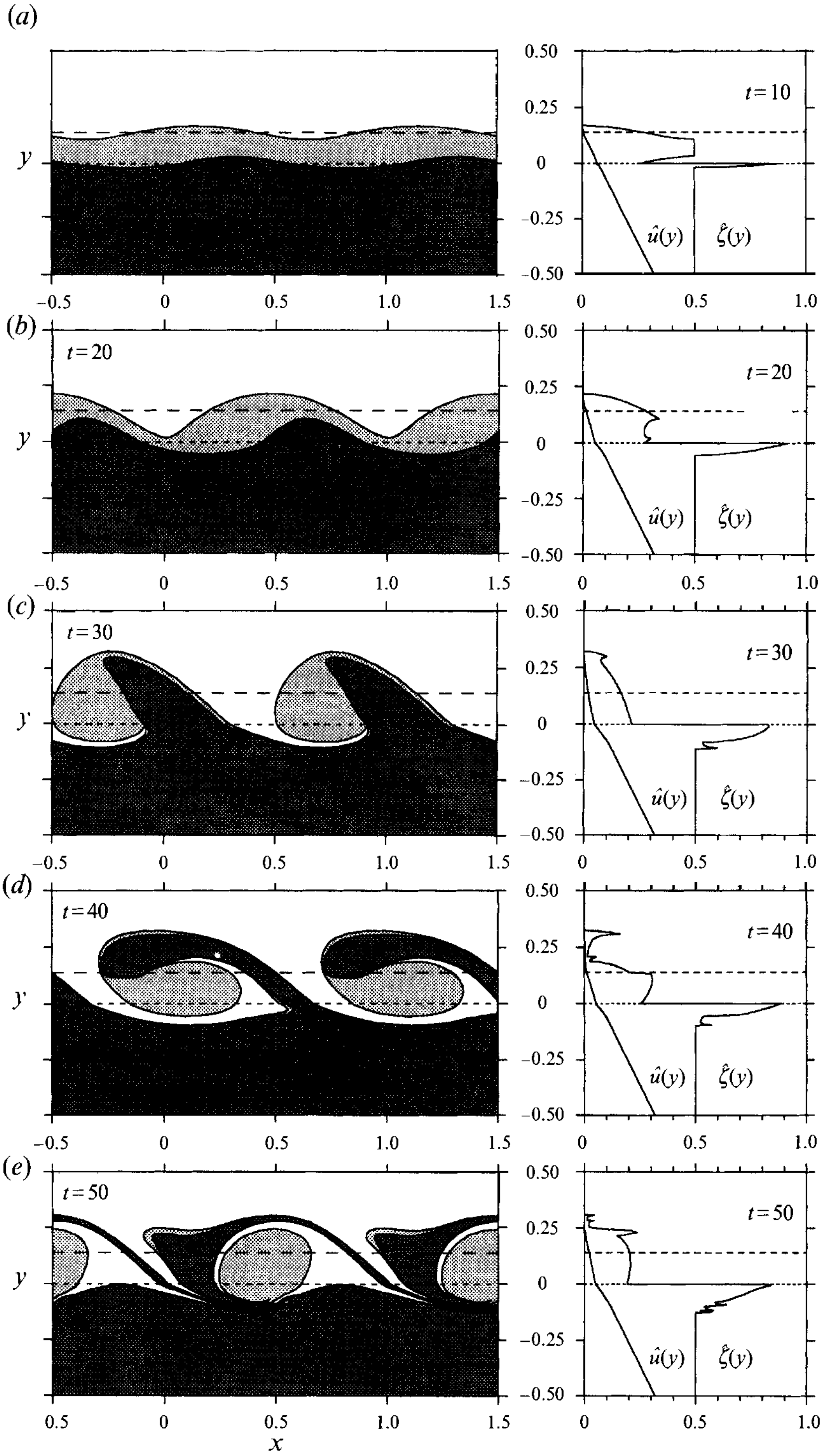

FIGURE 10. The evolution of the fastest growing mode for a given non-dimensional step height E, and Rossby number Ro ($E = 0.5$, $Ro = 0.5$). The product $(2\pi/\lambda)\, l_s$ and the amplitude ratio and phase shift between the two interfaces is prescribed by the linear theory. Thus if $\lambda = 1$, then the initial excursion of the shear flow on the shelf $l_s = 0.14$. The light shaded strip contains the maximum potential

derived from (A 15)) for given non-dimensional shear $Ro = \bar{\zeta}/f$ (or Rossby number) and cross-stream topographic change E. When a value for l_s is chosen, the wavelength λ of the disturbance is prescribed by the maximum growth rate of the linear analysis. In most runs the amplitude factor A was small enough ($\sim 10^{-2}$) to allow a comparison of the numerics with the linear theory, but no significant differences were noticed if somewhat different values are chosen; this will only alter the time required for the nonlinearities to be noticeable. Thus, only two parameters remain: E and Ro. For clarity, we will only discuss in detail cases with $E = 0.5$ because similar features were observed for other values of E (see figure 13 for the extent of the parameter range explored and computed).

When $Ro = E$, the potential vorticity of the irrotational ($y > l_s$) and deep region ($y < 0$) are equal (figure 10), and the early evolution (figure 10*a*) is as predicted by the linear theory with the crest and trough of each interface growing exponentially with time. Consistent with this growth is the phase shift between L_1 and L_2 which ensures that the positive vorticity anomalies in the L_1 crest induce a net 'upward' (amplifying) motion on the nearest L_2 crest and vice versa. As the disturbance gets larger (figure 10*b*), straining by the mean shear causes interfacial steepening ahead of the L_1 trough and behind the L_2 ridge, leading to the roll-up and core formation ($t > 30$), as in the classical Kelvin–Helmholtz problem (Pozrikidis & Higdon 1985). Figure 10(*c*) clearly shows the accumulation of high potential vorticity into well-defined cores along the escarpment whereas the maximum penetration of the disturbance in adjacent regions is limited. The emerging state, even though not strictly steady, seems to consist of cores (pools) of maximum potential vorticity, around which tongues of lesser-potential-vorticity fluid from the deep as well as from the irrotational shallow region wind (figure 10*d*, *e*). Also shown in figure 10 is the x-averaged relative vorticity distribution $\hat{\zeta}(y)$, obtained for any given y by finding the length of the horizontal segments intercepted by the various contours. The corresponding mean velocity distribution was obtained by integrating $\hat{\zeta}(y) = -\partial\hat{u}(y)/\partial y$. The amount of different water 'types' (fluid with different shading and potential vorticity) transported across the escarpment was also computed. Note that the pinching-off of the interfaces tends to trap 'deep' water on the shelf ($y > 0$). This water is partially replaced by high-potential-vorticity core water whose stretching accounts for the region of maximum mean vorticity at $y < 0$. This illustrates how a counter-gradient vorticity flux can maintain a maximum shear and oppose any type of diffusive action tending to reduce the peak value. The topographic instability in figure 10 may suggest a new statistically (x-averaged) steady state with maximum mean vorticity increased by 70%, and the small positive $\hat{\zeta}(y)$ at $y > l_s$ implies that deep water will always ($t > 0$) occupy the upper shelf region. (But the continual shoaling of the real continental topography would inhibit the spreading to large positive y, i.e. the 'beach' zone.) Likewise, filaments from the upper shelf are entrained near $0 < y < l_s$, would around the core and advected with the mean field far downstream from its place of origin on the upper shelf. The oceanographic significance of this water-type transport is discussed in the conclusion.

When Ro is increased (figure 11), with E and l_s constant, the most unstable λ is

---

vorticity and the two dashed lines represent the undisturbed frontal positions. The initial condition is given by (4.1) with $A = 10^{-2}$. The timescale is the reciprocal of the Coriolis parameter. The nonlinear effects are apparent at $t = 20$ (*b*) and lead to the formation of well-defined cores of uniform potential vorticity (light shaded areas) surrounded by entrained water from the deep region (dark shaded areas) and the irrotational region (*c*–*e*). In parallel with the evolution of the interfaces, the cross-stream vorticity distribution $\hat{\zeta}(y)$ and the along-escarpment velocity $\hat{u}(y)$ averaged over one wavelength are shown.

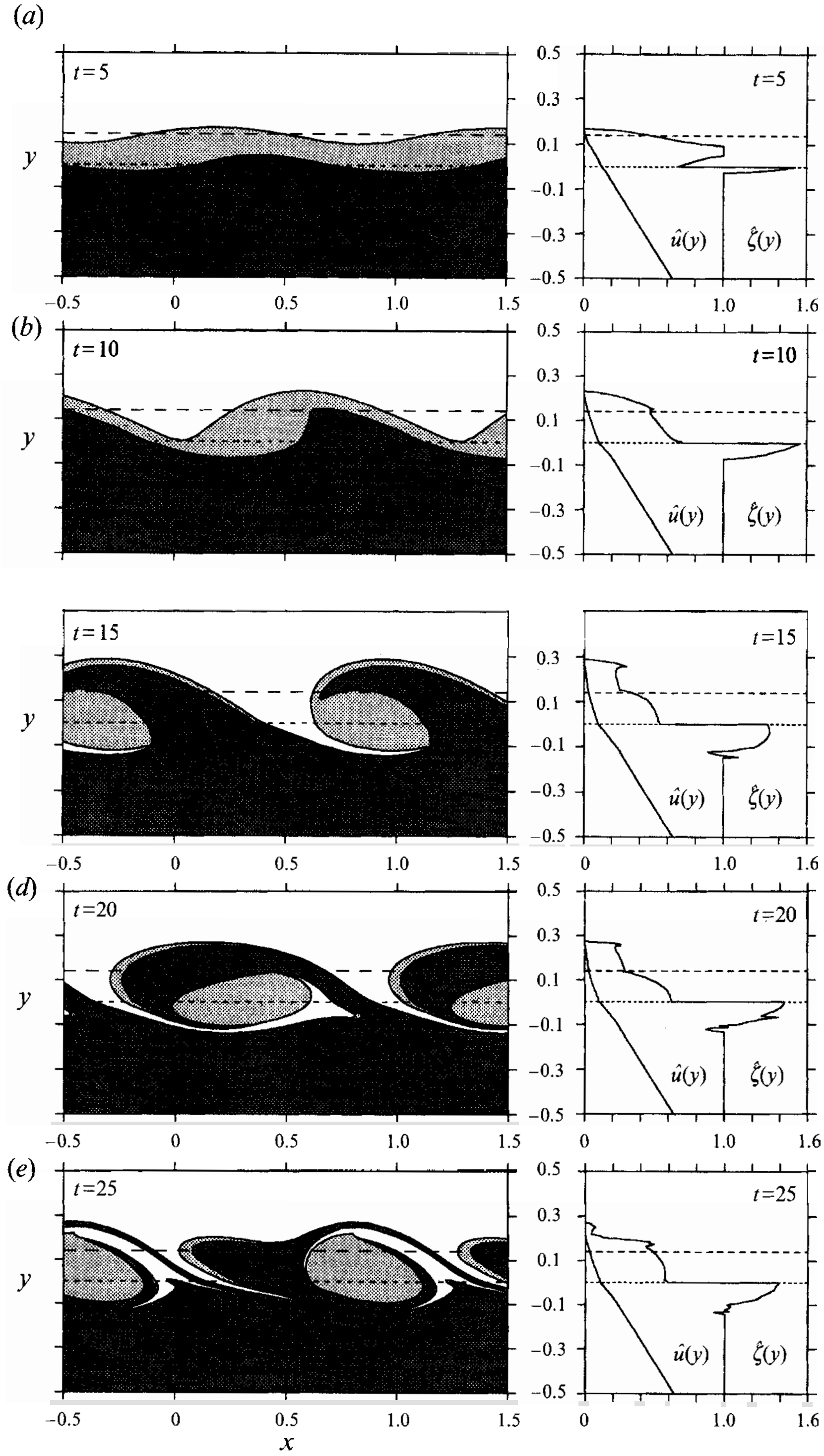

FIGURE 11 Similar to figure 10, except for $Ro = 1$, $\lambda = 1.25$ (same l_s), $A = 1.25\times 10^{-2}$. Note that less than two wavelengths are shown.

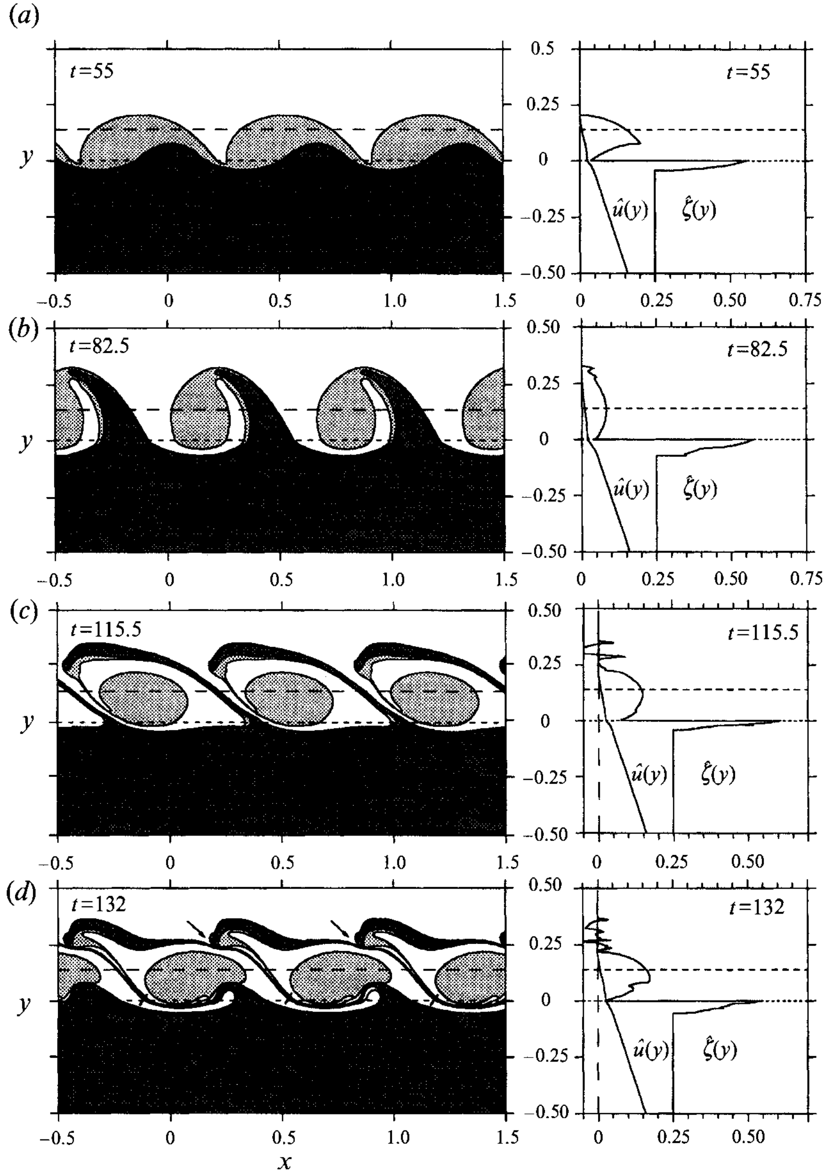

FIGURE 12. Similar to figure 10, except for $Ro = 0.25$, $\lambda = 0.65$ (same l_s), $A = 0.65 \times 10^{-2}$. Note that a little bit more than three wavelengths are shown.

increased and the linear growth rate is increased too. The stronger effect leads to more deep water per wavelength on the shelf (figure 11 *e*) than occurred previously, and less irrotational water is entrained around the eddy.

On the other hand, when $Ro < E$ (figure 12), the topographic restoring forces become stronger relative to the shear effect, and growth rate is reduced. Pooling still occurs but the emerging cores are now mainly surrounded by water which originated from the outer shelf region, whereas the portion of deep water transported across the shelf break is smaller than in figure 11. Note that in this case ($Ro < E$) the irrotational water crossing $y = 0$ acquires a greater relative vorticity than the undisturbed value, and thereby adds (along with the core water) to the increased mean vorticity (figure

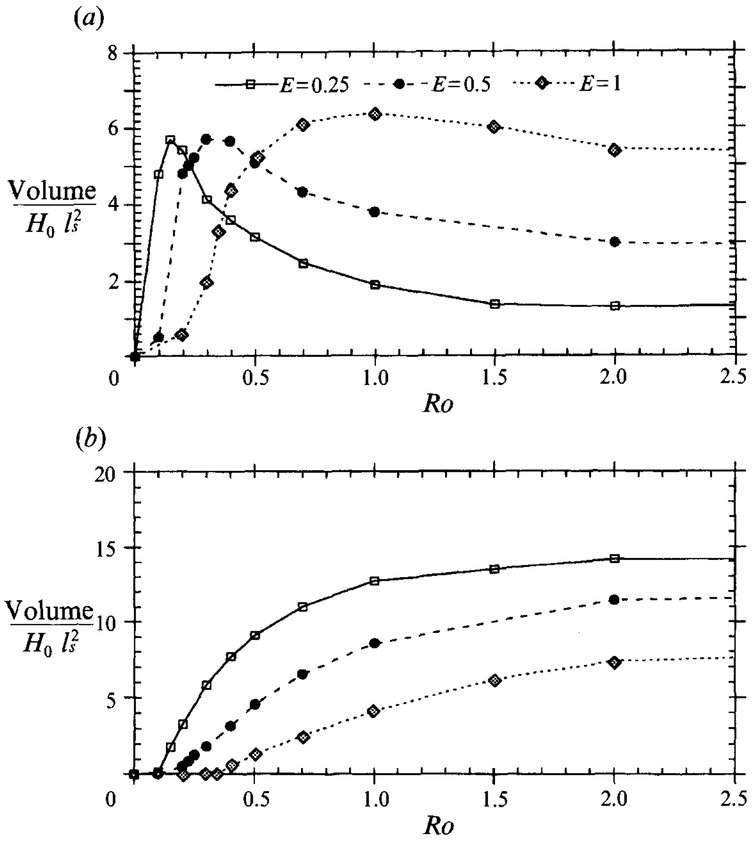

FIGURE 13. (*a*) Non-dimensional entrained volume per wavelength of irrotational shelf water into the shear flow (see text) and (*b*) non-dimensional volume transport of deep water across the shelf break as a function of *Ro* and *E* for the fastest growing normal mode and given l_s. The depth of the shallow region (H_0) was chosen as the vertical lengthscale in normalizing the volume (these values can be converted per unit downstream length but this was not done here because it spreads the curves further apart on the graph).

12*c*). But we can see that a smaller fraction of the cores appears at $y < 0$ thereby limiting the cross-stream extent of the region of maximum relative vorticity. Furthermore the cross-stream penetration of deep water onto the shelf is more pronounced even though its volume is smaller.

Many other cases were investigated for different values of *Ro* and *E* as indicated in figure 13 which shows the entrained volume of irrotational water per eddy into the shear layer, as well as the volume transport of deep water across the shelf break, as a function of those two parameters using normal modes with maximum growth rate and small initial amplitude at $t = 0$ for a given value of l_s (chosen such that $\lambda = 1$ when $E = Ro = 0.5$, figure 10). In each case, the depth of the shelf is the vertical lengthscale. The entrained volume was defined and computed as follows (Stern & Bidlot 1994). The branch of L_1 in the ridge of the amplifying wave (figure 12*b*) winds counterclockwise around the core, and approaches the trailing branch of L_1 in the trough of the wave. Close contact of the L_1 branches occurs at the arrows in figure 12(*d*), at which point a 'cut' is made to form a multiconnected L_1. One portion of this constitutes a 'new' shear flow interface, outside which is purely irrotational fluid and inside which are the cores plus the entrained irrotational fluid. In this study, the cut is made when and where the distance between the two corresponding branches is less than the average distance between successive Lagrangian points (e.g. in figure 12*d*, the cut was made at the arrows). The volume of irrotational water entrained inside the new L_1 interface is plotted in figure 13(*a*). Similarly (figure 12*b*), each ridge of the amplifying L_2 wave is squeezed at its base ($y = 0$) between two consecutive wedges of shelf water winding around the cores. This leads (figure 12*c*) to the pinching-off of a finite volume of deep water on the shelf. A cut was made in a manner similar to L_1 when the two branches were in close contact above $y = 0$ (see dashes in figure 12*d*) and the isolated volume defines the transport of deep water across the shelf break (figure 13*b*).

The limiting case of *Ro* going to infinity (achieved physically if the Coriolis parameter is set to zero) was calculated by changing the timescale to the reciprocal of the basic-state vorticity, and the values for the entrained volumes agree with extrapolations obtained from figure 13. For very small shear (figure 13), the initial distance (l_s) between the two fronts is large relative to the wavelength, thereby reducing the mutual interaction between the interfacial waves. Although nonlinearity causes the slowly amplifying L_1 wave to break, it never reaches $y = 0$. In that case, only a small portion of irrotational fluid is entrained in a manner similar to the study of 'shingle formation' at a single shear-layer interface (Stern 1985; Dritschel 1988). No wave breaking occurs for L_2, but rather a finite-amplitude topographic oscillation, similar to what would occur in a constant shear in $-\infty < y < +\infty$. The larger the step the stronger the shear needs to be to produce breaking.

When *Ro* is of order $\frac{1}{3}E$, cross-shelf transport (figure 13*b*) appears first as a long filament containing a small amount of deep water which winds around the cores, and then for larger *Ro* a larger volume is pinched off just above the escarpment, as shown in the three examples given above (figures 10–12). Figure 13(*a*) shows that for any given geometry, an increasing shear will first increase the amount of originally irrotational fluid that can be trapped inside the shear layer until a maximum is reached (around $Ro \sim 0.7$–$0.8E$), followed by slower decrease of the former amount. On the other hand (figure 13*b*), the exchange between the deep and the shelf region increases monotonically with the background shear.

As shown earlier the mean relative vorticity is increased to higher values than the corresponding background value through a counter-gradient vorticity flux. To characterize this we can look at the relative difference between the maximum average relative vorticity and the background value: $(\hat{\zeta}_{max}-\bar{\zeta})/\bar{\zeta}$ for $y \leqslant 0$, which is plotted in figure 14(*a*) for the three cases studied above. First note that the initial normal mode with infinitesimal $L_2(x,0) < 0$ produces a finite vorticity anomaly because of the escarpment discontinuity, and this immediately yields $(\hat{\zeta}_{max}-\bar{\zeta})/\bar{\zeta} = 0.5E(1+Ro)/Ro$. The increase in ordinate at $t > 0$ is due to the broadening at $y < 0$ of the corresponding cyclonic anomaly region (figures 10*b*, 11*b*, 12*a*). At later times (figure 14*a*) a sharp drop in $\hat{\zeta}_{max}$ occurs when originally irrotational shelf water is transported across the escarpment, replacing core water, thereby generating weaker vorticity anomalies. The evolution thereafter depends on the relative proportions of originally irrotational and core water on the deep side of the step. The dashed lines in figure 14(*a*) represent the time average over an interval which spans from $t = 0$ to t_e, the time at which a new L_1 interface has reformed. These average values are plotted (solid line) in figure 14(*c*) for the parameter range considered here. Note that even though the instantaneous maximum oscillates, the time average is approximately equal to the initial value. Therefore a larger step and/or a smaller shear will produce a larger relative increase in vorticity.

A useful measure of nonlinear finite amplitude is the width of the high-vorticity

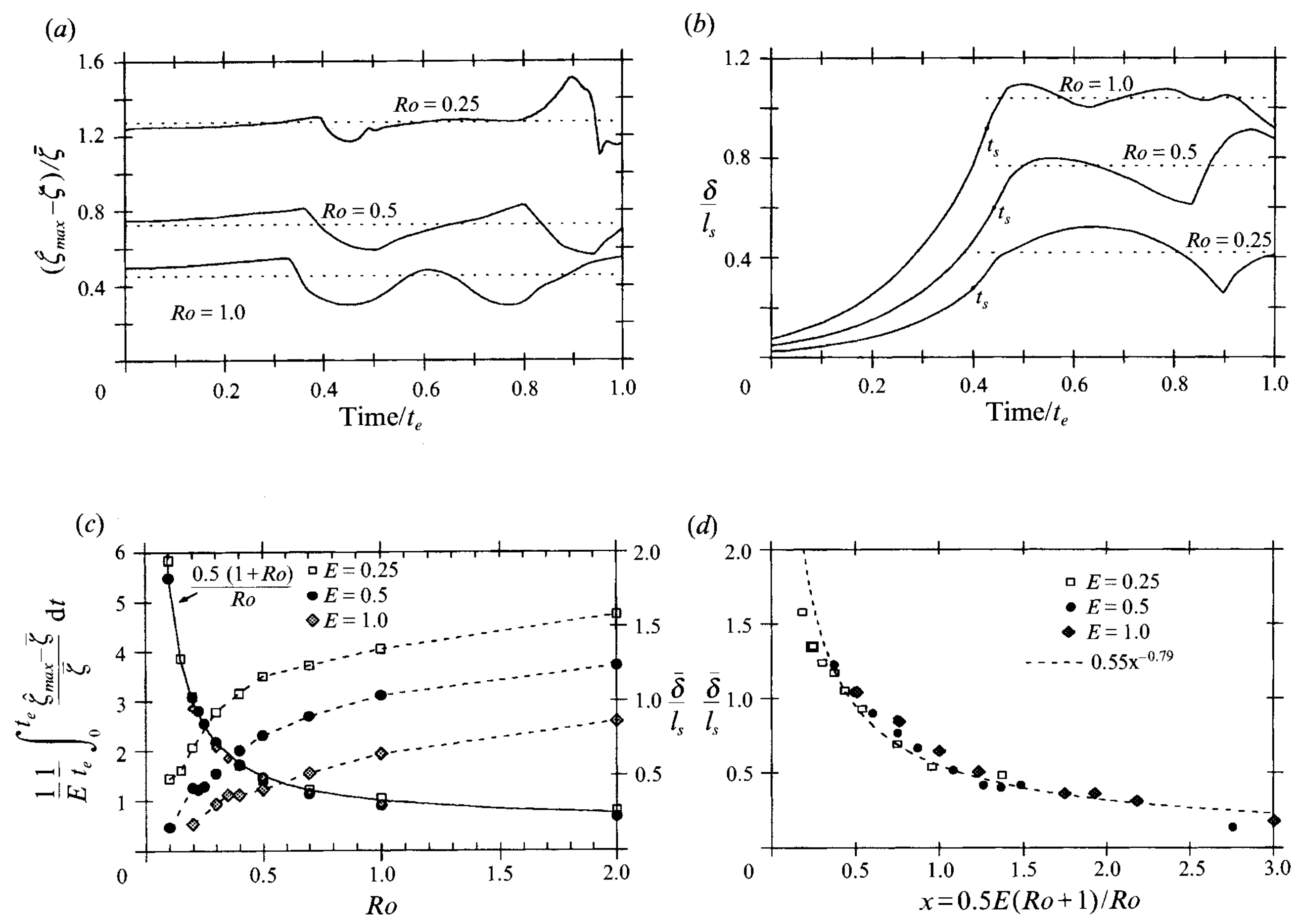

FIGURE 14. Some major properties of the instability. (*a*) Relative maximum in horizontally averaged relative vorticity ($\hat{\zeta}$) as a function of time for the three cases presented in figures 10–12; t_e is the entrainment time (see text); $E = 0.5$. The dotted lines are the average over the time interval in question. (*b*) Penetration distance (δ) of the disturbance into the deep region as function of t/t_e and l_s. The dotted lines are the average value from $t = t_s$ to $t = t_e$ (see text). $E = 0.5$. (*c*) Solid line (left ordinate): average relative maximum vorticity increase normalized by E. Dashed lines (right ordinate): average value of δ/l_s as a function of Ro. (*d*) Average value of δ/l_s as a function of Ro and E. The dashed line is the best power fit to the data.

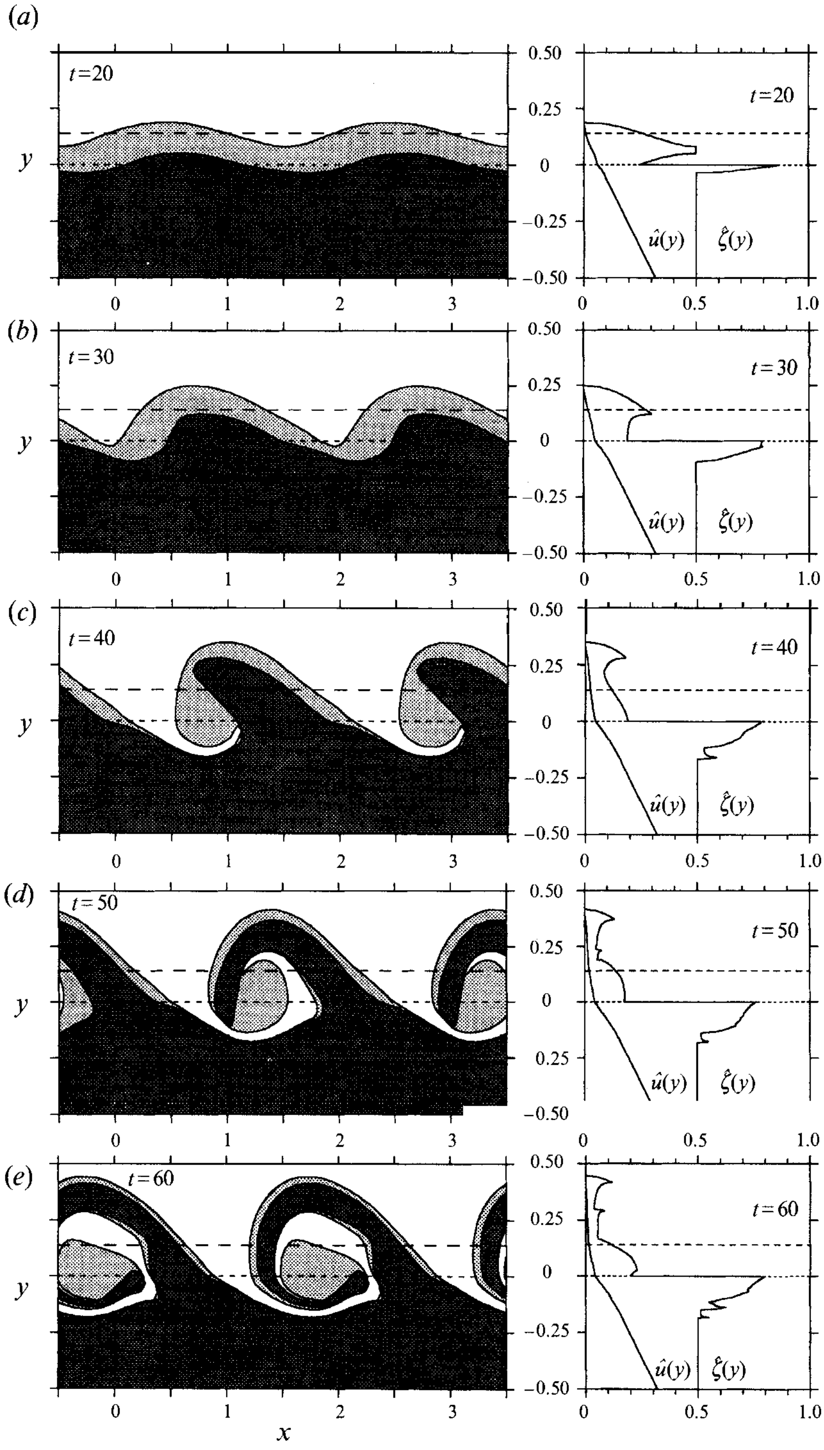

FIGURE 15. Same as figure 10, except for $\lambda = 2$ (i.e. the first harmonic is the most unstable wave). Note the scale distortion.

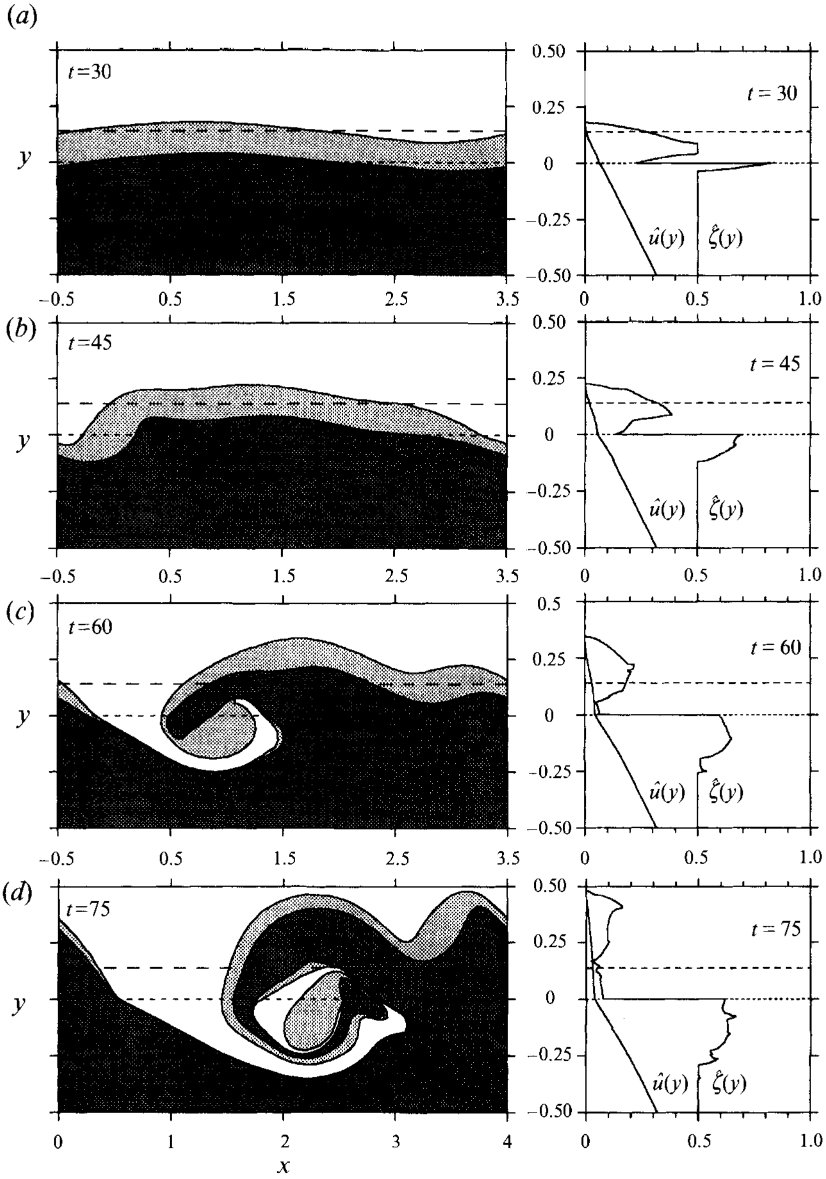

FIGURE 16. Same as figure 10, except for $\lambda = 4$ (i.e. the second harmonic is the linearly most unstable wave). Only one wavelength is shown. Note the scale distortion.

region δ, defined as the distance from $y = 0$ to the point $y < 0$ where the x-average total vorticity returns to its background value. Figure 14(*b*) shows the evolution of δ for the same three cases as before. The early growth ($t/t_e < 0.4$) extends well into the nonlinear regime until wave breaking produces distinct cyclonic cores and irrotational water returns on the shelf (figures 10*c*, 11*c*, 12*b*). At that point, δ levels off and its subsequent evolution follows the evolution of the cores as they oscillate across the step. A mean penetration $\bar{\delta}$ was defined by taking the average over $[t_s, t_e]$, where t_s is the earliest time at which the (exponentially) growing δ equals the minimum δ. For $Ro = 0.25$ (figure 14*b*) min δ occurs at time/$t_e = 0.9$ and $t_s/t_e \approx 0.4$. The dashed curves in figure 14(*c*) shows that $\bar{\delta}$ increases when the topographic constraint is relaxed (smaller E), and fluid columns crossing the escarpment can penetrate further in the deep region before curving back towards the shelf, thereby producing a wider region of high vorticity. The value of $\bar{\delta}/l_s$ increases with *Ro*, except for a localized minimum (dent) around $Ro \approx \frac{1}{3}E$, implying that instability of a stronger shear flow will result in a wider region of increased vorticity, even though a smaller relative maximum in vorticity occurs as already mentioned. A partial compaction of the dependence of $\bar{\delta}/l_s$ on *Ro* and *E* is given in the summary diagram (figure 14*d*).

5. Other initial conditions

In all previous runs the normal mode with maximum growth rate was used as initial condition. As in the study of geostrophic shear layers (Pratt & Pedlosky 1991), we may ask if the spacing between vortex cores is determined by the initialization λ. If we initialize the problem with one normal mode whose harmonics may have larger growth rate, then the primary wave may generate higher harmonics through nonlinear wave–wave interaction, and these harmonics may grow more rapidly even though they will have zero amplitude initially. We can view such a run as a competition experiment between a primary wave and its harmonics. In our case we can see from the linear calculations (figure 20) that not all modes are linearly unstable owing to the existence of a long-wave cut-off. We will focus on small initial disturbances and only consider unstable waves. This is the case when $E = Ro = 0.5$, for which the corresponding fastest growing mode was analysed in figure 10. A doubling of the wavelength to $\lambda = 2$ in (4.1) will result in an initial wave whose first harmonic has a wavelength equal to the fastest growing mode for the given geometry; note however that the initial condition only contains one mode, i.e. the primary one. As shown in figure 15, the overall evolution is qualitatively similar to the previous cases: the high-potential-vorticity fluid pooling into detaching eddies combined with mixing of irrotational and deep water. Note that once the different water types are fully wound around the cores, the scale is entirely dominated by the eddy spacing given by the primary wavelength ($\lambda = 2$). The entrainment process is stronger in this case for both water types, with a non-dimensional entrained volume of 14.8 and a transport of 17.3 compared (figure 13) respectively to 5.1 and 4.5 for the fastest growing normal mode. Furthermore, the perturbation penetrates deeper into the deep region (figure 14*c*) ($\bar{\delta}/l_s = 1.4$ compared to 0.77) but with smaller relative maximum in relative vorticity (0.62 versus 0.75). These stronger effects may be partially attributed to the larger wavelength, but the qualitative result stands even if we consider the entrained volume per unit downstream length.

When $\lambda = 4$ is selected as the primary wavelength. The competition is now between this wave, its first harmonic (the primary wave of the previous case), and its second harmonic (the fastest growing wave). The evolution of this mode is plotted in figure 16 (note that only one primary wavelength is shown). The calculation was stopped before the final entrainment stage could be recognized but as shown in figure 16(*d*) a large amount of 'deep' water has penetrated on the shelf with the primary cores straddled over the escarpment, thereby generating a substantial region of maximum vorticity ($\bar{\delta}/l_s \approx 2.5$) with a smaller relative maximum value (≈ 0.4). Notice that signs of the shorter-wave spectrum are visible as secondary bulges emerge; however primary cores, spaced by a distance equal to the primary wavelength, subsequently dominate the evolution by wrapping and straining these secondary eddies around the cyclonic cores.

Following Pratt & Pedlosky, another type of competition experiment can be achieved by initiating a run with two waves having equal growth rate but different phase structure. In this case the initial condition is given by

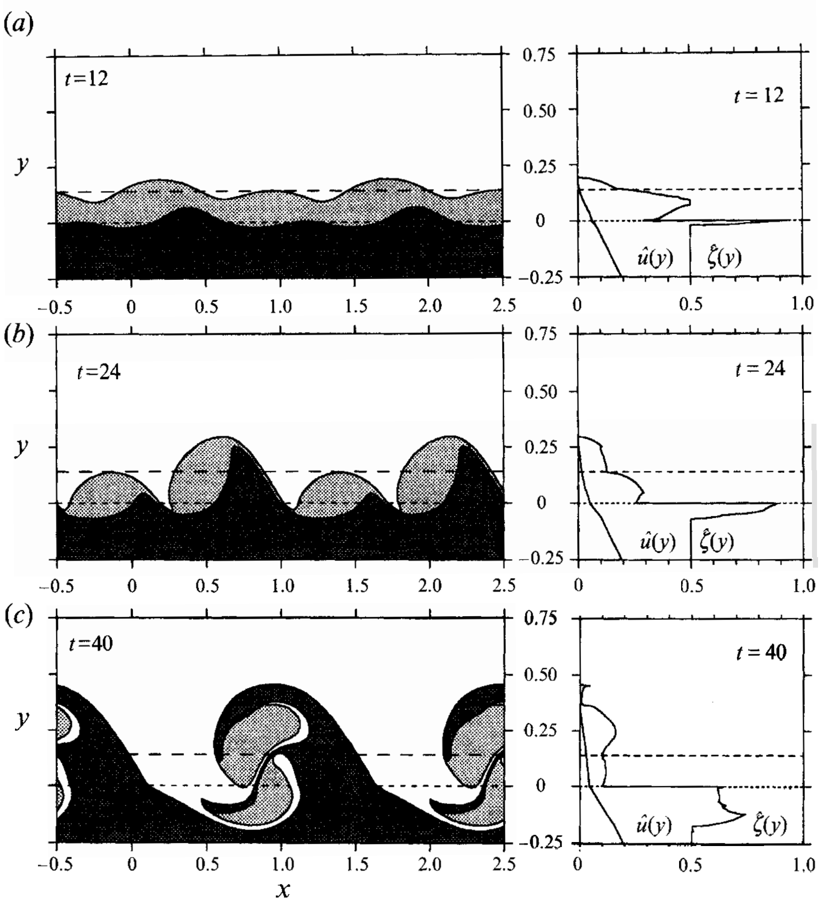

FIGURE 17. Competition experiment between two normal modes of equal growth rate with wavelengths given by $\lambda_1 = 1.5318$ and $\lambda_2 = \frac{1}{2}\lambda_1$ and zero phase lag between them.

$$\left.\begin{aligned} L_1 &= l_s + A\cos\left(\frac{2\pi}{\lambda_1}x\right) + A\cos\left(\frac{2\pi}{\lambda_2}x+\theta_0\right), \\ L_2 &= AA_1\cos\left(\frac{2\pi}{\lambda_1}x+\theta_1\right) + AA_2\cos\left(\frac{2\pi}{\lambda_2}x+\theta_2+\theta_0\right), \end{aligned}\right\} \tag{5.1}$$

where A_1 and θ_1, and A_2 and θ_2 are respectively the amplitude and the phase shift as given by the linear theory for the first and second waves. θ_0 is the adjustable phase of the second wave relative to the first. As before we select the two waves in the same unstable regime and geometry. If $\lambda_1 = 1.5318$ and $\lambda_1 = \frac{1}{2}\lambda_2$, then the two waves have the same growth rate (figure 20). The phase shift θ_0 is set to zero initially. The presence (figure 17*a*, *b*) of both wavelengths is evident in the first stage and the core spacing is equivalent to the shortest wavelength. But the subsequent evolution (figure 17*c*) leads to the merger of consecutive cores and produces a net increase in the mixing ability of the flow by forcing a deeper penetration of the disturbance into the adjacent regions. It is interesting to note that this result generalizes the instability theory applied to a vortex street structure (Saffman & Schatzman 1982) since the λ_1 wave can be viewed as a sub-harmonic perturbation to the periodic vortex distribution with spacing λ_2. For such a case we can expect the vortices to merge with their neighbours to form a larger-scale structure with wavelength λ_1. Similar features appear when the phase lag θ_0 is varied (not shown), but the orientation and staggering of the pools differs from figure 17.

6. Conclusions and suggestions

We have computed the finite-amplitude evolution of a non-inflected shear flow destabilized by a cross-stream variation of topography, in order to illustrate an apparently ubiquitous effect in continental boundary currents, namely the counter-gradient vorticity flux, or the increase in maximum mean vorticity, as summarized in figure 14. This effect is to be contrasted with the rapid diffusion of mean vorticity which would occur in the barotropic instability of a flow (figure 2) without topography, and in which the relative vorticity was conserved. The same kind of vorticity diffusion would occur (independent of mechanism) in any classical (dispersive) parametrization of the effect of the eddies on the mean flow.

The applicability of our model to real continental boundary currents is limited by the absence of stratification and other kinds of topographic effects (e.g. Bane 1983). However, the oceanic isopycnals tend to have a similar cross-stream variation as the isobaths, and the relevant oceanic eddies conserve potential vorticity; so that the counter-gradient vorticity flux (figure 14) may be rather insensitive to the mechanism by which the eddies are generated and evolve. It is suggested that those potential-vorticity-conserving effects maintain such strong inshore lateral shears as is observed in the Gulf Stream. We also note the well-known rectification effect of baroclinic instability in the atmospheric jet stream (Pedlosky 1987) in which counter-gradient momentum (as well as vorticity) effects occur.

The simple escarpment model has also been used to illustrate the cross-slope transfer of conservative water mass properties like potential vorticity (fluids with different shadings in all our figures), temperature, salinity and nutrient in the more realistic oceanic case. Figure 12(*d*) for example, shows how an instability leads to the formation of a 'new' potential vorticity interface across which there has been entrainment of the 'inshore water mass', and figure 13 documents some of the volumetric transfers.

For further information about the oceanic processes alluded to, see the literature connected with frontal eddies observed at the edge of the Gulf Stream along the coast of the Southeastern United States (Vukovich *et al.* 1979; Zantopp, Leaman & Lee 1987; Lee *et al.* 1985, 1991) and at the edge of the Kuroshio as it flows along the steep continental slope of the East China Sea (Sugimoto *et al.* 1988; Qiu *et al.* 1990). Such frontal eddies are characterized by alternating tongues of cold and warm water which may originate from onshore or offshore advection as well as upwelling, see figure 4 in Lee *et al.* 1991 for a schematic representation of Gulf Stream frontal eddies as well as the satellite images found in Vukovich (figures 1–3), Lee *et al.* (colour plate 1) and Zantopp *et al.* (figures 3–6). These perturbations travel downstream and evolve through various stages. When the growth seems to have stopped, the cold water tongue is advected back to the shelf-trapping warm water on the shelf (figure 3 in Vukovich *et al.*). During all stages a large portion of the eddies remains on the shelf, the rest, generally part of the cold tongue, is advected in the stream (figure 11 in Sugimoto *et al.*).

The idealized escarpment model might also be used in interpreting numerical results obtained from *continuous* barotropic models. In that context, and for order of magnitude purposes, l_s might be associated with the cross-stream width of the potential vorticity maximum in the continuous model, $\bar\zeta$ might be associated with its maximum shear, and ΔH might be associated with $l_s\, \partial h_0/\partial y$, where $\partial h_0/\partial y$ is a typical continental slope, Then figure 14(*c*) should provide an estimate of the penetration depth ($\bar\delta$) of the vorticity anomaly, and the latter should be of order of $f\bar\delta\, \partial h_0/\partial y/h_0$. It is also interesting to speculate on the role of $\bar\delta$ as a 'mixing length', indicative of the degree to which water masses of different properties are brought into such close contact that much smaller 'turbulent' processes are initiated, including classical vorticity diffusion. This could reestablish a new unstable state leading to a new instability and to further entrainment of irrotational shelf water into the shear flow.

This work was supported by the Office of Naval Research, grant 1368-632-27.

Appendix A. Linear instability theory for figure 6

For smooth mean flow $\bar u$ and topography h (figure 1), the linearized potential vorticity equation for small-amplitude waves (prime quantities) with complex phase speed c and wavelength $2\pi/\lambda$ can first be written as

$$(\bar u - c)\frac{\partial \zeta'}{\partial x} + v'\frac{\partial \bar\zeta}{\partial y} - v'\frac{f+\bar\zeta}{h}\frac{\mathrm{d}h}{\mathrm{d}y} = 0, \tag{A 1}$$

where

$$\zeta' = \frac{\partial v'}{\partial y} - \frac{\partial u'}{\partial x}. \tag{A 2}$$

If M denotes the mass transport function then

$$hu' = -\frac{\partial M}{\partial y} \quad \text{and} \quad hv' = +\frac{\partial M}{\partial x}. \tag{A 3}$$

In figure 6, the unperturbed shear flow with constant vorticity is

$$\bar u = \begin{cases} 0, & y > l_s \\ \bar\zeta(l_s - y), & y < l_s \end{cases} \tag{A 4}$$

and

$$h = \begin{cases} H_m(1-r), & y > 0 \\ H_m(1+r), & y < 0, \end{cases} \tag{A 5}$$

where H_m is the mean depth, $r = E/(2+E)$, and $E = \Delta H/H_0$.

The discontinuity at $y = 0$ and l_s require the specification of connecting conditions, and conservation of mass across $y = 0$ can be expressed as

$$[M] = 0. \tag{A 6}$$

where [ ] denotes the jump discontinuity across the PV-interface in question.

The second matching condition for M is found by integrating (A 1) for a continuous field and then taking the limit. When u' and v' are eliminated using (A 2), and (A 3) the result for $y = 0$ or $y = l_s$ can be written as

$$(\bar u - c)\left[\frac{1}{h}\frac{\partial M}{\partial y}\right] + M\left[\frac{1}{h}\bar\zeta\right] + fM\left[\frac{1}{h}\right] = 0. \tag{A 7}$$

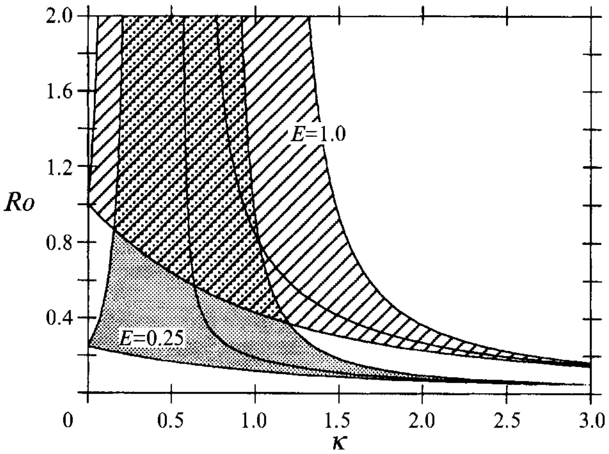

FIGURE 18. Non-dimensional wavenumber κ for the marginally stable and the fastest growing waves as a function of the Rossby number *Ro* for given values of the non-dimensional step height *E*. The shaded areas bounded by the marginally stable curves indicate the unstable regions.

At $y = l_s$ where the depth is continuous this becomes

$$-c\left[\frac{\partial M}{\partial y}\right]_{l_s^-}^{l_s^+} + M(l_s)[\bar{\zeta}]_{l_s^-}^{l_s^+} = 0, \tag{A 8}$$

and at $y = 0$ where the background vorticity is continuous we get

$$(\bar{\zeta} l_s - c)\left[\frac{1}{h}\frac{\partial M}{\partial y}\right]_{0-}^{0+} + (f+\bar{\zeta})\,M(0)\left[\frac{1}{h}\right]_{0-}^{0+} = 0. \tag{A 9}$$

In each region where the background vorticity and the fluid depth are constant M is a harmonic function. The solution for a normal mode is

$$M(x,y) = \hat{M}(y)\,\mathrm{e}^{\mathrm{i}kx}, \quad k > 0, \tag{A 10}$$

$$\hat{M}(y) = \begin{cases} \mathrm{e}^{-k(y-l_s)}, & y \geqslant l_s \\ \cosh(k(y-l_s)) + A\sinh(k(y-l_s)), & 0 \leqslant y \leqslant l_s \\ [\cosh(kl_s) - A\sinh(kl_s)]\,\mathrm{e}^{ky}, & y \leqslant 0, \end{cases} \tag{A 11}$$

where (A 6) has been used. The constant A satisfying (A 8) is

$$A = (\bar{\zeta}/kc) - 1. \tag{A 12}$$

The last connecting condition (A 9) yields the dispersion relationship. After some algebra this reduces to a quadratic equation for $1/c$, which can be written in non-dimensional form as

$$\beta^2\{\kappa(\mathrm{e}^{\kappa} + r\mathrm{e}^{-\kappa}) - rF(\mathrm{e}^{\kappa} - \mathrm{e}^{-\kappa})\} + \beta\{(2rF - 1 - 2\kappa)\,\mathrm{e}^{\kappa} - r\mathrm{e}^{-\kappa}\} + 2\mathrm{e}^{\kappa} = 0, \tag{A 13}$$

where

$$\beta = \frac{\bar{\zeta}}{kc}, \quad \kappa = kl_s, \quad F = \frac{f}{\bar{\zeta}} + 1 = \frac{1}{R_0} + 1, \quad R_0 = \frac{\bar{\zeta}}{f} \tag{A 14}$$

and where β gives the reciprocal phase speed.

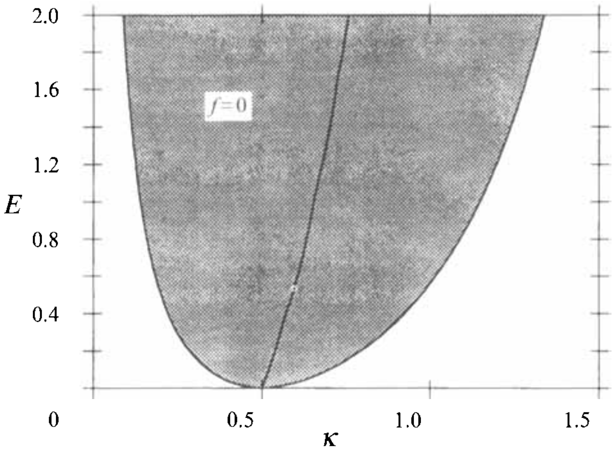

FIGURE 19. Non-dimensional wavenumber κ for the marginally stable and the fastest growing waves as a function of the non-dimensional step height E when the Coriolis parameter $f = 0$. The shaded area indicates the unstable region.

Figure 18 shows a plot of the non-dimensional wavenumber (κ) for the marginally stable waves as well as the fastest growing one as a function of the Rossby number Ro (non-dimensional shear) for different values of the step height (E). The shaded areas indicate the unstable regime. Except when $E = Ro$, there is a short- and a long-wave cut-off. In the case $E < Ro$, i.e. the background potential vorticity of the deep region is less than the corresponding value in the irrotational region on the shelf, the width of the unstable region decreases as Ro decreases. It can be shown that in the limit of large F (small shear) the unstable band behaves like rF. On the other hand, when $Ro > E$, increasing Ro will reduce the unstable bandwidth. In the limit $f = 0$, the flow is still unstable as shown in figure 19 as soon as a step is present ($E > 0$).

By linearizing the kinematic relationship which links the cross-escarpment velocity $v' = (1/h)(\partial M/\partial x)$ to the total time derivative of the ordinate of any point on one of the two interfaces ($L_1(x,t), L_2(x,t)$), it can be shown that the ratio of their complex amplitudes is

$$\frac{L_2^+}{L_1} = \frac{\cosh(\kappa) - (\beta - 1)\sinh(\kappa)}{1 - \beta\kappa} \tag{A 15}$$

and

$$\frac{L_2^-}{L_2^+} = \frac{1-r}{1+r} = \frac{1}{1+E}, \tag{A 16}$$

where the superscripts + or − indicate respectively a positive or negative L_2. Note that the slope of L_2 is discontinuous at $y = 0$ but the phase shift with respect to L_1 is the same for both positive and negative L_2. The expressions (A 15) and (A 16) were used to determine the initial condition for the contour dynamical computations.

Finally figure 20 shows typical growth rate curves (kc_i *vs.* κ) when the shear is varied for a given topography. Also shown is the phase shift between the two PV-interfaces. For long waves (small κ) the phase lag is close to zero and at the short-wave cut-off, the two interfaces are phase lagged by 180° (π). Note that for unstable waves, L_1 lags behind L_2 in a matter that favours growth of the disturbance through motion induced by the vorticity anomalies created when the PV-interfaces are disturbed.

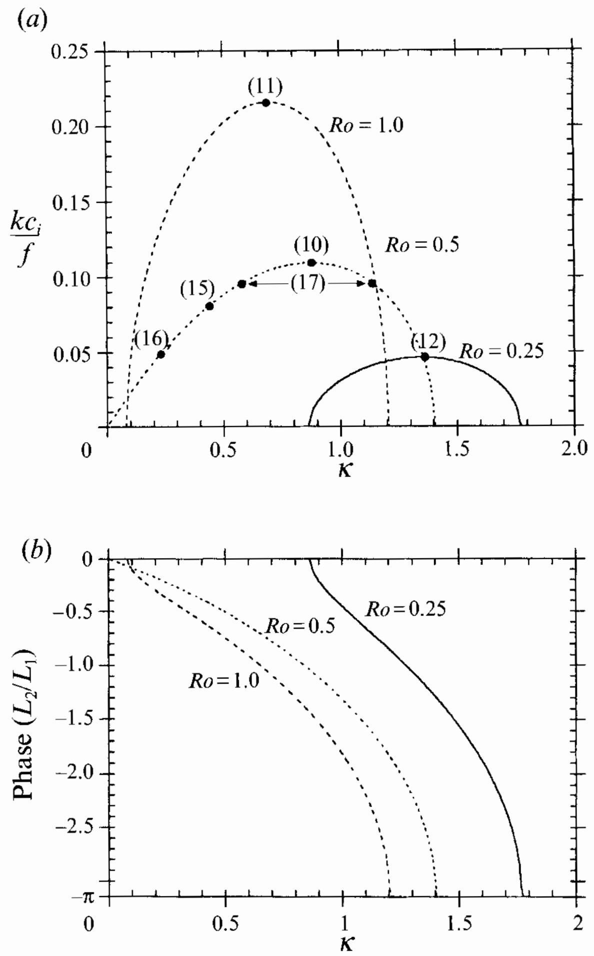

FIGURE 20. (*a*) Non-dimensional growth rate kc_i/f versus the non-dimensional wavenumber $\kappa = (2\pi/\lambda)\, l_s$ for different values of the Rossby number *Ro* and a given topography ($E = 0.5$). The numbers in parentheses refer to the figure's numbers showing the nonlinear evolution of those waves. (*b*) Phase lag between the normal mode along $y = l_s$ and $y = 0$ versus κ for different values of *Ro* and a given topography $E = 0.5$.

Appendix B. Velocity components for §3

The velocity components in problem 2 are obtained by differentiating (3.3)–(3.4), i.e.

$$[u_{2i}(x,y), v_{2i}(x,y)] = \left[-\frac{\partial \psi_{2i}}{\partial y}, \frac{\partial \psi_{2i}}{\partial x} \right], \quad i = 0, 1.$$

The linearity of the argument of $G(x-\xi, y-\eta)$ allows the permutation of the derivative variables x and y respectively with $-\xi$ and $-\eta$, and Green's theorem can be used to transform the corresponding area integrals into contour integrals along the entire $L_2(\xi)$ and $y = 0$ over one wavelength. These can be written as

$$u_{20}(x,y) = \frac{-1}{4\pi} E(\bar{\zeta}+f) \int_0^\lambda S(L_2(\xi)) \ln \frac{\sin^2((\pi/\lambda)(x-\xi)) + \sinh^2((\pi/\lambda)(y-L_2(\xi)))}{\sin^2((\pi/\lambda)(x-\xi)) + \sinh^2((\pi/\lambda)y)} \mathrm{d}\xi, \tag{B 1}$$

$$v_{20}(x,y)=\frac{-1}{4\pi}E(\bar{\zeta}+f)\int_0^{\lambda}S(L_2(\xi))$$
$$\times\ln\left[\sin^2((\pi/\lambda)(x-\xi))+\sinh^2((\pi/\lambda)(y-L_2(\xi)))\right]\mathrm{d}L_2(\xi), \quad \text{(B 2)}$$

$$u_{21}(x,y)=\frac{+1}{4\pi}E(\bar{\zeta}+f)\frac{E}{2+E}\int_0^{\lambda}\operatorname{sgn}[L_2(\xi)]\,S(L_2(\xi))$$
$$\times\ln\frac{\sin^2((\pi/\lambda)(x-\xi))+\sinh^2((\pi/\lambda)(|y|+|L_2(\xi)|))}{\sin^2((\pi/\lambda)(x-\xi))+\sinh^2((\pi/\lambda)y)}\mathrm{d}\xi, \quad \text{(B 3)}$$

$$v_{21}(x,y)=\frac{-1}{4\pi}E(\bar{\zeta}+f)\frac{E}{2+E}\operatorname{sgn}(y)\int_0^{\lambda}S(L_2(\xi))$$
$$\times\ln\left[\sin^2((\pi/\lambda)(x-\xi))+\sinh^2((\pi/\lambda)(|y|+|L_2(\xi)|))\right]\mathrm{d}L_2(\xi), \quad \text{(B 4)}$$

$$S(L_2(\xi))=\begin{cases}1/(1+E), & L_2(\xi)>0\\ 1, & L_2(\xi)<0.\end{cases} \quad \text{(B 5)}$$

Similarly, differentiating (3.5) in problem 1 will yield contour integrals along the entire $L_1(\xi), y=l_s$ and that portion of $y=0$ which intersects L_1 (figure 9). The resulting integrals are

$$u_{1i}(x,y)=\frac{1}{4\pi}\bar{\zeta}cu_i\int_0^{\lambda}\ln\frac{\sin^2((\pi/\lambda)(x-\xi))+\sinh^2((\pi/\lambda)(y-\eta_i(L_1(\xi))))}{\sin^2((\pi/\lambda)(x-\xi))+\sinh^2((\pi/\lambda)(y-\eta_i(l_s)))}\mathrm{d}\xi$$
$$+\frac{1}{4\pi}\bar{\zeta}E\int_{(\text{for }L_1(\xi)<0)}\ln\frac{\sin^2((\pi/\lambda)(x-\xi))+\sinh^2((\pi/\lambda)(y-\eta_i(L_1(\xi))))}{\sin^2((\pi/\lambda)(x-\xi))+\sinh^2((\pi/\lambda)y)}\mathrm{d}\xi, \quad \text{(B 6)}$$

where $L_1(\xi)<0$ means that the contour integration is only performed where $L_1(\xi)$ is negative, recall that $i=0$ corresponds to the constant-depth contribution, and $i=1$ the image contribution, and

$$cu_i=\begin{cases}1, & i=0\\ -E/(2+E), & i=1,\end{cases} \quad \text{(B 7)}$$

$$\eta_i(\eta)=\begin{cases}\eta, & i=0\\ -\eta\operatorname{sgn}(\eta)\operatorname{sgn}(y), & i=1.\end{cases} \quad \text{(B 8)}$$

Similarly we get

$$v_{1i}(x,y)=\frac{1}{4\pi}\bar{\zeta}ce_i\int_0^{\lambda}\ln\left[\sin^2((\pi/\lambda)(x-\xi))+\sinh^2((\pi/\lambda)(y-\eta_i(L_1(\xi))))\right]\mathrm{d}L_1(\xi)$$
$$+\frac{1}{4\pi}\bar{\zeta}E\,ce_i\int_{(\text{for }L_1(\xi)<0}\ln\left[\sin^2((\pi/\lambda)(x-\xi))+\sinh^2((\pi/\lambda)(y-\eta_i(L_1(\xi))))\right]\mathrm{d}L_1(\xi), \quad \text{(B 9)}$$

where

$$ce_i=\begin{cases}1, & i=0\\ E\operatorname{sgn}(y)/(2+E), & i=1.\end{cases} \quad \text{(B 10)}$$

Finally, (B 1), (B 2), (B 3), (B 4), (B 6) and (B 9) can be used in (3.8) to evaluate the total velocity components due to the vorticity anomalies.

Appendix C. Numerical considerations

The numerical technique used here is similar to the one in Stern (1985, 1991*b*), namely the integral-differential equations (3.10) are reduced to a large number of ordinary differential equations by introducing discrete Lagrangian points along the interfaces. The velocity components were computed using a trapezoidal approximation to the integrals, with, as usual, indentation at the logarithmic singularity in the expression for u_{m0}, v_{m0}, $m = 1,2$((B 1), (B 2), (B 6), (B 9)) where an analytical approximation similar to Stern & Pratt (1985) was used since the integration of the periodic Green's function over a small interval surrounding the logarithmic singularity can be reduced to a form identical to their non-periodic counterpart.

New features were added to deal with numerical problems due to the depth discontinuity at $y = 0$. Because of this, the interfacial slopes are discontinuous at $y = 0$ and a higher resolution in Lagrangian points near $y = 0$ was required. Furthermore the integrands in (B 1)–(B 4) are discontinuous at $y = 0$ and the exact position where $y = 0$ intersects $L_1(x, t)$ is needed to evaluate the integrals in (B 6) and (B 9). For these reasons, the intersection of the contours with $y = 0$ was necessary for an accurate evaluation of those contour integrals. Several interpolation schemes were tried and the simpler one was retained. This involved a simple linear interpolation between the closest Lagrangian point on each side of the corresponding intersection with $y = 0$. In the same context, when the Lagrangian points were the only integration nodes in the trapezoidal quadrature to the integral in (B 3), a poor approximation was obtained if $|L_2(\xi, t)| \ll 1$, because the integrand in (B 3) varies rapidly over a small interval of order of a few Lagrangian point spacings. Indeed, when $|L_2(\xi, t)| \ll 1$, the integrand behaves like ln (2) if $\xi = x, y = L_2(\xi)$, but if the integration variable $(\xi, L_2(\xi))$ is not in the close neighbourhood of $(x, L_2(x))$, the integrand behaves like $\ln(1) = 0$. This problem is particularly acute at the earliest stages of the evolution of a small-amplitude disturbance, and can be alleviated if a function is added and subtracted to the integrand. The resulting integrand can be split into an analytically integrable part and a smoother function which can be integrated more accurately with the usual trapezoidal quadrature. Namely, if (x_j, L_j) denotes any Lagrangian point on L_2 then the integrand in (B 3) can be smoothed out by subtracting a function $g(x_j, L_j, \xi)$ that can be analytically integrated. Thus we can rewrite (B 3) as

$$u_{21}(x_j, L_j) = \frac{1}{4\pi} E(\bar{\zeta}+f)\frac{E}{2+E}$$

$$\times\left\{\mathrm{Int}+\int_0^\lambda \left[\operatorname{sgn}(L_2(\xi))\, S(L_2(\xi)) \ln\frac{\sin^2((\pi/\lambda)(x_j-\xi))+\sinh^2((\pi/\lambda)(|L_j|+|L_2(\xi)|))}{\sin^2((\pi/\lambda)(x_j-\xi))+\sinh^2((\pi/\lambda)\, L_j)}\right.\right.$$

$$\left.\left. -g(x_j, L_j, \xi)\right] \mathrm{d}\xi\right\},$$

where

$$g(x_j, L_j, \xi) = \operatorname{sgn}(L_j)\, S(L_j) \ln\frac{\sin^2((\pi/\lambda)(x_j-\xi))+\sinh^2((\pi/\lambda)2L_j)}{\sin^2((\pi/\lambda)(x_j-\xi))+\sinh^2((\pi/\lambda)\, L_j)}$$

and Int is its exact integral:

$$\mathrm{Int} = \int_0^\lambda g(x_j, L_j, \xi)\, \mathrm{d}\xi = 2\pi S(L_j)\, L_j.$$

A similar procedure can be used for the first integrand in ((B 6), $i = 1$). Unfortunately, the second integrals in that expression cannot be reduced to a known integral. The same applies to (B 4) and ((B 9), $i = 1$). Once again the integrands in those integrals vary rapidly over a small interval which straddles the Lagrangian point where the integrals are evaluated if this point is close to $y = 0$. A local increase in point resolution was found to grasp most of the variation and was applied by using extra integration nodes, linearly interpolated between the three successive Lagrangian points defining the interval over which the integrand varies the most. These integration nodes are just computational artefacts and never appear in the array describing the interfaces.

A second-order Runge–Kutta scheme was used in the temporal integration of the periodic disturbance, except for Lagrangian points which cross $y = 0$ over a given time step. In this case, the second-order scheme incurs excessive errors because of the cross-escarpment velocity discontinuity, and therefore the following procedure was used. The time step $\Delta t = \Delta t_1 + \Delta t_2$ was split into two parts, where Δt_1 is the time taken by (say) a deep-water parcel to go at constant speed $v > 0$ from $y = L < 0$ to $y = 0$. Then the velocity was changed according to (2.1), and the new v was used to compute the displacement in the remaining time interval Δt_2. A similar procedure was used for a parcel at $y = L > 0$ which crosses the escarpment in one time step. No such treatment was necessary for the x-component of the Lagrangian parcel.

To maintain proper resolution along the contours a slightly modified version of Meacham's (1991) point rearrangement scheme was used. Also, long filaments with negligible area were smoothed out automatically in an attempt to keep the number of Lagrangian nodes as low as possible.

A preliminary check of the initial velocity field as well as the evolution of the periodic disturbance was obtained by using as initial condition a normal mode from the linear analysis with small amplitude, and by comparing the results with their linear counterparts like velocity components, growth rate, and phase speed (Appendix A). Stokes theorem was used to check the accuracy of the velocity field for larger disturbances, by computing the circulation around any closed curve in the region of interest and comparing the result with the integrated vorticity enclosed by that curve. The errors in entrainment volume could be ascertained by monitoring errors in conserved quantities like the volume bounded by each interface and $y = 0$.

REFERENCES

Bane, J. M. 1983 Initial observation of the subsurface and short-term variability of the seaward deflection of the Gulf Stream off Charleston, South Carolina. *I. Geophys. Res.* **88** (C8), 4673–4684.

Bidlot, J. R. 1993 Contour dynamical study of the barotropic instability of continental boundary currents. PhD dissertation, Florida State University.

Brooks, D. A., & Mooers, C. 1977 Free, stable continental shelf waves in a sheared, barotropic boundary current. *J. Phys. Oceanogr.* **7**, 380–388.

Brooks, I. H. & Niiler, P. P. 1977 Energetics of the Florida current. *J. Mar. Res.* **35**, 163–191.

Collings, S. I. & Grimshaw, R. 1980 The effect of topography on the stability of a barotropic coastal current. *Dyn. Atmos. Oceans* **5**, 83–106.

Collings, S. I. & Grimshaw, R. 1984 Stable and unstable barotropic shelf waves in a coastal current. *Geosphys. Astrophys. Fluid Dyn.* **29**, 179–220.

Dritschel, D. G. 1988 The repeated filamentation of two-dimensional vorticity interfaces. *J. Fluid Mech.* **194**, 511–547.

Ford, W. L., Longard, J. R. & Banks, R. E. 1952 On the nature, occurrence and origin of cold low salinity water along the edge of the Gulf Stream. *J. Mar. Res.* **11**, 281–293.

Grimshaw, R. & Yi, Z. 1991 Evolution of a potential vorticity front over a topographic slope. *J. Phys. Oceanogr.* **21**, 1240–1255.

KOZLOV, V. F. 1983 The method of contour dynamics in model problems of ocean topographysical cyclogenesis. *Izv. Atmos. Ocean. Phys.* 635–640.

LAMB, H. 1932 *Hydrodynamics*. Dover.

LEE, T. N. & ATKINSON, L. P. 1983 Low frequency current and temperature variability from Gulf Stream frontal eddies and atmospheric forcing along the South East U.S. outer continental shelf. *J. Geophys. Res.* **88** (C8), 4541–4567.

LEE, T. N., KOURAFALOU, V., WANG, J. D., HO, W. J., BLANTON, J. O., ATKINSON, L. P. & PIETRAFESA, L. J. 1985 Shelf circulation from Cape Canaveral to Cape Fear during winter. In *Oceanography of the Southeastern U.S. Continental Shelf, Coastal and Estuarine Science Series*, vol. 2 (ed. L. P. Atkinson, D. W. Menzel & K. A. Bush), pp. 33–61. Washington DC: AGU.

LEE, T. N. & MAYER, D. A. 1977 Low-frequency current variability and spin-off eddies along the shelf off Southeast Florida. *J. Mar. Res.* **35**, 193–220.

LEE, T. N., YODER, J. A. & ATKINSON, L. P. 1991 Gulf Stream frontal eddy influence on productivity of the Southeast U.S. continental shelf. *J. Geophys. Res.* **96** (C12), 22191–22205.

MEACHAM, S. P. 1991 Meander evolution on piecewise-uniform, quasi-geostrophic jets. *J. Phys. Oceanogr.* **21**, 1139–1170.

PEDLOSKY, J. 1987 *Geophysical Fluid Dynamics*, 2nd edn. Springer.

POZRIKIDIS, C. & HIGDON, J. J. 1985 Nonlinear Kelvin–Helmholtz instability of a finite vortex layer. *J. Fluid Mech.* **157**, 225–263.

POZRIKIDIS, C. & HIGDON, J. J. 1987 Instability of compound vortex layer and wakes. *Phys. Fluids* **30**, 2965–2975.

PRATT, L. J. & PEDLOSKY, J. 1991 Linear and nonlinear instability of geostrophic shear layers. *J. Fluid Mech.* **224**, 49–76.

QIU, B., TODA, T. & IMOSATO, N. 1990 On Kuroshio front fluctuations in the East China Sea using satellite and in situ observational data. *J. Geophys. Res.* **95** (C10), 18191–18204.

SAFFMAN, P. G. & SCHATZMAN, J. C. 1982 Stability of a vortex street of finite vortices. *J. Fluid Mech.* **117**, 171–185.

SEND, U. 1989 Vorticity and instability during flow reversals on the continental shelf. *J. Phys. Oceanogr.* **19**, 1620–1633.

SPITZ, Y. H. & NOF, D. 1991 Separation of boundary currents due to bottom topography. *Deep-Sea Res.* **38**, 1–20.

STERN, M. E. 1985 Lateral wave breaking and 'shingle' formation in large-scale shear flow. *J. Phys. Oceanogr.* **15**, 1274–1283.

STERN, M. E. 1991*a* Countergradient vorticity flux generated in continental boundary currents. *J. Phys. Oceanogr.* **21**, 1622–1630.

STERN, M. E. 1991*b* Entrainment of an eddy at the edge of a jet. *J. Fluid Mech.* **228**, 343–360.

STERN, M. E. 1993 Topographic jetogenesis and transitions in straits and along continents. *J. Phys. Oceanogr.* **23**, 843–854.

STERN, M. E. & BIDLOT, J.-R. 1994 Lateral entrainment in baroclinic currents. *J. Mar. Res.* **52**, 25–53.

STERN, M. E. & PRATT, L. J. 1985 Dynamics of vorticity fronts. *J. Fluid Mech.* **161**, 513–532.

SUGIMOTO, T., KIMURA, S. & MIYAJI, K. 1988 Meander of the Kuroshio frontal variability in the East China Sea. *J. Oceangr. Soc. Japan* **44**, 125–135.

THOMPSON, L. 1993 Two-layer quasi-geostrophic flow over finite isolated topography. *J. Phys. Oceanogr.* **23**, 1297–1314.

VUKOVICH, F. M., CRISSMAN, B. W., BUSHNELL, M. & KING, W. J. 1979 Gulf Stream boundary eddies off the East Coast of Florida, *J. Phys. Oceanogr.* **9**, 1214–1222.

WANG, X. 1992 Interaction of an eddy with a continental slope. PhD thesis, MIT/WHOI Joint Program in Oceanography.

ZABUSKY, N. J., HUGHES, M. H. & ROBERTS, K. V. 1979 Contour dynamics for the Euler equations in two dimensions. *J. Comput. Phys.* **30**, 96–106.

ZANTOPP, R. J., LEAMAN, K. D. & LEE, T. N. 1987 Florida Current meanders: a close look in June–July 1984. *J. Phys. Oceanogr.* **17**, 584–595.